

1-1-1989

A two-dimensional numerical model of the high electron mobility transistor

Sze-Him Ng

University of Nevada, Las Vegas

Follow this and additional works at: <https://digitalscholarship.unlv.edu/rtds>

Repository Citation

Ng, Sze-Him, "A two-dimensional numerical model of the high electron mobility transistor" (1989). *UNLV Retrospective Theses & Dissertations*. 28.

<http://dx.doi.org/10.25669/r07q-alao>

This Thesis is protected by copyright and/or related rights. It has been brought to you by Digital Scholarship@UNLV with permission from the rights-holder(s). You are free to use this Thesis in any way that is permitted by the copyright and related rights legislation that applies to your use. For other uses you need to obtain permission from the rights-holder(s) directly, unless additional rights are indicated by a Creative Commons license in the record and/or on the work itself.

This Thesis has been accepted for inclusion in UNLV Retrospective Theses & Dissertations by an authorized administrator of Digital Scholarship@UNLV. For more information, please contact digitalscholarship@unlv.edu.

INFORMATION TO USERS

The most advanced technology has been used to photograph and reproduce this manuscript from the microfilm master. UMI films the text directly from the original or copy submitted. Thus, some thesis and dissertation copies are in typewriter face, while others may be from any type of computer printer.

The quality of this reproduction is dependent upon the quality of the copy submitted. Broken or indistinct print, colored or poor quality illustrations and photographs, print bleedthrough, substandard margins, and improper alignment can adversely affect reproduction.

In the unlikely event that the author did not send UMI a complete manuscript and there are missing pages, these will be noted. Also, if unauthorized copyright material had to be removed, a note will indicate the deletion.

Oversize materials (e.g., maps, drawings, charts) are reproduced by sectioning the original, beginning at the upper left-hand corner and continuing from left to right in equal sections with small overlaps. Each original is also photographed in one exposure and is included in reduced form at the back of the book. These are also available as one exposure on a standard 35mm slide or as a 17" x 23" black and white photographic print for an additional charge.

Photographs included in the original manuscript have been reproduced xerographically in this copy. Higher quality 6" x 9" black and white photographic prints are available for any photographs or illustrations appearing in this copy for an additional charge. Contact UMI directly to order.

U·M·I

University Microfilms International
A Bell & Howell Information Company
300 North Zeeb Road, Ann Arbor, MI 48106-1346 USA
313/761-4700 800/521-0600

Order Number 1337608

**A two-dimensional numerical model of the high electron
mobility transistor**

Ng, Sze-Him, M.S.

University of Nevada, Las Vegas, 1989

U·M·I
300 N. Zeeb Rd.
Ann Arbor, MI 48106

A TWO-DIMENSIONAL NUMERICAL MODEL OF
THE HIGH ELECTRON MOBILITY
TRANSISTOR

by

Sze-Him Ng

A thesis submitted in partial fulfillment
of the requirements for the degree of

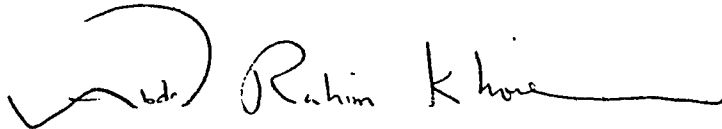
Master of Science

in

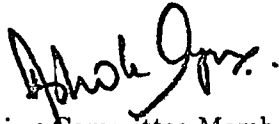
Electrical Engineering

Department of Computer Science and
Electrical Engineering
University of Nevada, Las Vegas
May, 1989

The thesis of Sze-Him Ng for the degree of Master of Science in
Electrical Engineering is approved.

A handwritten signature in black ink, appearing to read "Abdol Rahim Khoie". The signature is fluid and cursive, with a large initial "A" and "R".

Chairperson, Abdol Rahim Khoie, Ph. D.

A handwritten signature in black ink, appearing to read "Ashok Iyer". The signature is cursive and somewhat compact.

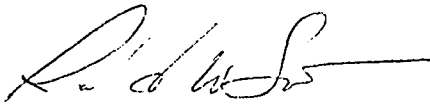
Examining Committee Member, Ashok Iyer, Ph. D.

A handwritten signature in black ink, appearing to read "S. Singh". The signature is cursive and somewhat stylized.

Examining Committee Member, S. Singh, Ph. D.

A handwritten signature in black ink, appearing to read "Rohan Dalpatadu". The signature is cursive and somewhat complex.

Graduate Faculty Representative, Rohan Dalpatadu, Ph. D.

A handwritten signature in black ink, appearing to read "Ronald W. Smith". The signature is cursive and somewhat simple.

Graduate Dean, Ronald W. Smith, Ph. D.

University of Nevada, Las Vegas
May, 1989

Abstract

A two-dimensional numerical model of the high electron mobility transistor (HEMT) with consideration of quantization in the channel is presented. In previous numerical models of the HEMT, the quantization was treated by means of a triangular well approximation which approximates the variation of the electrostatic potential in the quantum well by a linear relationship. Electrons were assumed to reside right at the heterojunction and completely screen the electric field induced by the gate voltage. In this model, we do not make the above assumptions. Instead, the spatial spread of the electron concentration in the quantum well normal to the heterojunction is taken into consideration by solving Schrödinger's and Poisson's equations self-consistently. The Boltzmann transport equation in the form of a current continuity equation and an energy transport equation is solved to obtain the transient transport behavior. Transport of carriers takes place in two layers in the GaAs region: the lowest subband of the quantum well and a non-quantized bulk layer. Electrons in the quantum well travel in one direction along the heterojunction, whereas electrons in the bulk layer travel in all directions on the two-dimensional simulation plane. A finite difference scheme based on a non-uniform rectangular mesh is used to solve the system of equations.

The simulation program developed has been used on a number of device structures to investigate the effects on the overall performance of the device due to variation of the gate length and the impurity doping concentration in AlGaAs. It has been found that a reduction in the gate length results in an increase of the drain current which is partly due to a shift in the threshold

voltage. An increase in the drain current can also be obtained by having a higher doping level, in which case the transconductance is also expected to increase.

Contents

Acknowledgement	i
Abstract	ii
Table of Contents	iv
List of Figures	vi
List of Symbols	ix
1 Introduction	1
2 Overview of HEMT Models	4
2.1 Basic System of Equations	4
2.2 Charge Control Models	6
2.3 Numerical Models	8
2.4 Monte Carlo Simulations	11
3 Our Numerical Approach	13
3.1 Device Structure	13
3.2 Transport	14
3.3 The Quantum Well	16
3.4 Solution of Schrödinger's Equation	19
3.5 Boundary Conditions	24
3.6 Numerical Stability Consideration	26

	v
3.7 Discretization Scheme	27
3.8 Transport Parameters	30
4 Results	31
4.1 Drain Current Drain Voltage Characteristic	32
4.2 Drain Current Gate Voltage Characteristic	34
4.3 Effects of the Gate Length	37
4.4 Effects of Doping	37
5 Discussion and Conclusion	39
Table	42
Figures	43
Reference.	76

List of Figures

1.1	Formation of the 2DEG in GaAs	43
3.1	Device structure	44
3.2	Linearized potential well	45
3.3	Electrostatic potential	46
4.1	Electrostatic potential along the source boundary	47
4.2	Electron concentration along the source boundary	48
4.3	A typical wavefunction taken at a cross-section of the con- ducting channel	49
4.4	Energy subbands in the quantum well	50
4.5	Drain current drain voltage characteristics for Device II . . .	51
4.6	Electrostatic potential with a gate voltage of 0.7V and a drain voltage of 0.5V	52
4.7	Electrostatic potential with a gate voltage of 0.7V and a drain voltage of 1.35V	53
4.8	Electron concentration in the bulk with a gate voltage of 0.7V and a drain voltage of 0.5V	54
4.9	Electron concentration in the bulk with a gate voltage of 0.7V and a drain voltage of 1.35V	55
4.10	Electron concentration in the quantum well with a gate volt- age of 0.7V and a drain voltage of 0.5V	56

4.11	Electron concentration in the quantum well with a gate voltage of 0.7V and a drain voltage of 1.35V	57
4.12	Transverse current density with a gate voltage of 0.7V and a drain voltage of 0.5V	58
4.13	Transverse current density with a gate voltage of 0.7V and a drain voltage of 1.35V	59
4.14	Longitudinal current density with a gate voltage of 0.7V and a drain voltage of 0.5V	60
4.15	Longitudinal current density with a gate voltage of 0.7V and a drain voltage of 1.35V	61
4.16	Total electron concentration in Device II with a gate voltage of 0.25V and a drain voltage of 0.9V	62
4.17	Total electron concentration in Device II with a gate voltage of 0.5V and a drain voltage of 0.9V	63
4.18	Total electron concentration in Device II with a gate voltage of 0.75V and a drain voltage of 0.9V	64
4.19	Total electron concentration in Device II with a gate voltage of 1.0V and a drain voltage of 0.9V	65
4.20	Total electron concentration in Device II with a gate voltage of 1.25V and a drain voltage of 0.9V	66
4.21	Transient currents for Device II with a gate voltage of 0.5V and a drain voltage of 0.9V	67
4.22	Drain current-gate voltage characteristic for Devices I-V under a drain voltage of 1.0V	68
4.23	Charge-gate voltage characteristic for Devices I-V under a drain voltage of 1.0V	69

4.24	Transconductance for Devices I-V under a drain voltage of 1.0V	70
4.25	Gate capacitance for Devices I-V under a drain voltage of 1.0V	71
4.26	Unity-gain frequencies for Devices I-V under a drain voltage of 1.0V	72
4.27	Variation of transconductance with the gate length	73
4.28	Variation of transconductance with the doping level	74
4.29	Average energy for Device VI with a gate voltage of 0.35V and a drain voltage of 1.0V	75

List of Symbols

ϵ	permittivity
μ	electron mobility
μ_E	energy flux mobility
Φ_{MS}	work function difference between metal and semiconductor
ψ_i	wavefunction for the i -th subband
τ_{HF}	high frequency factor
$Ai(\cdot)$	Airy function
C_g	gate capacitance
D	diffusivity
D_E	energy flux diffusivity
E	average electron energy
E_{F_n}	quasi-Fermi energy in the quantum well
E_i	the i -th eigenvalue for the quantum well
ΔE_c	conduction band discontinuity
E_G	energy bandgap of AlGaAs
G	redistribution factor
G_{bulk}	redistribution factor for the bulk
G_I	redistribution factor for the quantum well
G_n	electron generation rate
G_p	hole generation rate
I_D	drain current
N_C	effective density of states in the bulk
N_{I_C}	effective density of states in the quantum well
N_D	n-type impurity doping level

$U(x)$	potential energy
U_n	electron recombination rate
U_p	hole recombination rate
V	electrostatic potential
V_{bi}	built-in voltage
V_D	drain voltage
V_G	gate voltage
V_S	source voltage
T_L	lattice temperature
g_m	transconductance
f_T	unity-gain frequency
\hbar	Planck's constant
\mathbf{j}	total current density
\mathbf{j}_n	electron current density
\mathbf{j}_p	hole current density
k	Boltzmann constant
m_x	electron conduction effective mass
n	electron concentration
q	electronic charge
s	energy flux
t	time

Chapter 1

Introduction

Ultra-fast electronics is one of the main focus of advanced research in semiconductors. A high-speed device which has drawn much attention in recent years is the High Electron Mobility Transistor (HEMT). The same device has been called by different researchers under names such as MODFET, TEGFET, and SDHT [1],[2],[3]. HEMT works under the principle of the field effect transistor (FET) in which the current in the device is controlled by the electric field induced by the gate voltage.

HEMT differs from other FET devices in that the accumulation of carriers in the conduction channel is due to the heterostructure of the device. A heterostructure consists of layers of materials having different energy bandgaps. The junction between two layers is called a heterojunction. The most commonly used materials for HEMT are GaAs and AlGaAs because of their closely matched lattice structures. Advanced fabrication technology developed in recent years makes possible the technique of modulation doping in which the AlGaAs layer is heavily doped with donor impurities and the GaAs layer is kept undoped. As the free electron in AlGaAs has higher energy than that in GaAs, transfer of electrons from AlGaAs to GaAs takes

place, resulting in an accumulation of charge in GaAs. The discontinuity of the conduction band at the heterojunction acts as a barrier to the movement of free electrons in GaAs, forming a potential well (Fig. 1.1). The well is normally narrow enough to confine the electron and quantization effects become considerable. Discrete energy levels, or subbands, are formed in the quantum well. Electrons in the quantum well experience restricted dimensionality in their motion, and transport takes place in a two-dimensional plane parallel to the heterojunction. Thus, electrons in the quantum well form a two-dimensional electron gas (2DEG).

One distinctive feature of the 2DEG is that electrons are physically separated from their donor impurities in AlGaAs. An undoped spacer layer is usually added between the highly doped AlGaAs layer and the quantum well to further separate the impurities from the heterojunction. As a result, electron scattering due to impurities in the crystal is greatly reduced, giving rise to high mobility. Ultra-high-speed switching times, 5.8 ps at 77K and 10.2 ps at 300K, have been demonstrated for AlGaAs/GaAs HEMT's [4], [28].

Despite its high-speed performance, HEMT suffers from a tight control of the threshold gate voltage which is normally restricted to within 1V [5]. As the gate voltage is further increased, the performance is severely degraded due to a sharp decrease of the transconductance. The transconductance reveals information as to how fast the channel current responds to a change in the gate voltage. Leakage current through the Schottky barrier at the gate under high gate voltage can become unacceptably high [29], [30]. It has been shown [29] that the gate voltage swing can be increased by adding a layer of highly doped p-type GaAs right under the gate. In an ideal situation, transport of carriers takes place only in the quantum well. However,

under high drain voltages, electrons gain enough energy to escape from the quantum well, resulting in parallel conduction in the bulk GaAs and Al-GaAs regions. In order to better understand the physics of the device and to identify areas where the performance of HEMT is hampered, analytical and numerical studies are often carried out.

In this thesis, a two-dimensional numerical model of HEMT will be presented. Chapter 2 outlines various mathematical models that have been developed. Chapter 3 introduces our approach to the modeling of the device and the numerical procedure involved. Chapter 4 gives the results of our simulation. Further discussion and conclusions are given in Chapter 5.

Chapter 2

Overview of HEMT Models

HEMT models based on analytical or numerical techniques have been developed in order to acquire a better understanding of the device physics, to predict the performance of the device under certain operating conditions, and to draw insights from the result on device design. In this chapter, three different approaches to HEMT modeling are reviewed: the Charge Control Model, the Numerical Model and the Monte Carlo Simulation.

2.1 Basic System of Equations

The general problem one deals with in a HEMT model is the transport of charge carriers through a medium of varying electrostatic potential. To obtain the potential profile, one needs to solve Poisson's equation

$$\nabla^2 V = \frac{q}{\epsilon}(n - p + N_A - N_D) \quad (2.1)$$

where q is the electronic charge, ϵ is the permittivity, n is the electron concentration, p is the hole concentration, N_A is the acceptor doping level, and N_D is the donor doping level. In most cases, the hole concentration is assumed to be zero.

As for transport, carriers are treated as classical particles in which the time of interaction is much shorter than the time between interaction. The motion of such particle is described by the Boltzmann equation

$$\frac{\partial f}{\partial t} = -\frac{1}{\hbar} \nabla_{\mathbf{k}} E(\mathbf{k}) \cdot \nabla f - \frac{q}{\hbar} \mathbf{F} \cdot \nabla_{\mathbf{k}} f + \left. \frac{\partial f}{\partial t} \right|_{col} \quad (2.2)$$

where $f = f(\mathbf{r}, \mathbf{k}, t)$ is the particle density in real and momentum space, \mathbf{F} is the electric field, \mathbf{r} is the positional vector, \mathbf{k} is the wavevector, and the last term is a collision term

$$\left. \frac{\partial f}{\partial t} \right|_{col} = \frac{V}{8\pi^3} \int \{S(\mathbf{k}, \mathbf{k}')f(\mathbf{k})[1 - f(\mathbf{k}')] - S(\mathbf{k}', \mathbf{k})f(\mathbf{k}')[1 - f(\mathbf{k})]\} d\mathbf{k} \quad (2.3)$$

where V is the total volume of the material, and $S(\mathbf{k}, \mathbf{k}')$ is the scattering rate of a particle undergoing transition from state \mathbf{k} to state \mathbf{k}' . Analytical solution for the Boltzmann equation can be obtained only for certain special cases and in general numerical methods are used. One approach is the Monte Carlo method which simulates the random motion of particles in semiconductor materials by generating random numbers which approximate the scattering probability of electrons [13]. Another approach is to use the integrated form of the Boltzmann equation, or the Boltzmann moment equations, which are expressed in terms of macroscopic quantities such as the electron concentration, current density, average energy, and energy flux.

The quantum system in HEMT is described by Schrödinger's equation

$$-\frac{\hbar^2}{2m} \frac{d^2 \psi_i}{dx^2} + U(x) \psi_i = E_i \psi_i \quad (2.4)$$

where m is the electron conduction effective mass, U is the potential energy, ψ_i is the wavefunction, and E_i is the eigenvalue. Since Schrödinger's equation involves the electrostatic potential, and the electrostatic potential, in turn, depends on the electron distribution, obtaining an accurate electron

density in a quantum system requires a self-consistent solution of Poisson's and Schrödinger's equations. Most HEMT models that treat the quantum system use the triangular well approximation [6], [8], [21] in which the electric field in the quantum well is assumed constant. The eigenvalues under this approximation are given by

$$E_i = \left(\frac{\hbar^2}{2m} \right)^{1/3} \left(\frac{3}{2} \pi q F \right)^{2/3} \left(i + \frac{3}{4} \right)^{2/3} \quad (2.5)$$

where F is the electric field in the quantum well. The electron population in each subband is governed by the Fermi-Dirac statistics

$$N_i = \frac{mkT}{\pi \hbar^2} \ln \left[1 + \exp \left(-\frac{E_i - E_F}{kT} \right) \right] \quad (2.6)$$

where E_F is the Fermi energy.

2.2 Charge Control Models

The earliest theoretical study on HEMT is based on the so-called Charge Control Model [7]. A number of studies have been reported using this approach [8], [9], [10]. The main idea of the model is to derive analytically the relationship between various external voltages and the charge density in the channel from which the current-voltage characteristics and the capacitance-voltage characteristics can be obtained. Since the mathematical expressions involved are relatively simple, computational effort required is minimal.

The basic assumption in this approach is a gradual channel approximation: The electric field normal to the heterojunction is assumed to be much greater than the electric field perpendicular to the heterojunction. Thus, Poisson's equation which solves for the electrostatic potential in the device can be reduced to a one-dimensional equation involving only the dominant

field in the perpendicular direction

$$\frac{d^2V}{dx^2} = -\frac{q}{\epsilon}N(x) \quad (2.7)$$

where $N(x)$ is the impurity doping level. Electrons in the conduction channel are assumed to occupy only the lowest subband and completely screen the electric field induced by the gate potential. A triangular well approximation based on constant electric field in the quantum well is used to calculate the energy level of the subband and the corresponding electron population. Carrier heating and two-dimensional effects of electron transport are usually not taken into account, whereas velocity overshoot and saturation may be included in the model by taking a proper velocity-field relationship.

The relationship between the gate voltage and the sheet charge n_s in the channel is obtained by integrating Poission's equation, yielding,

$$n_s = \frac{\epsilon}{q^2d}(qV_g' - qV_c) \quad (2.8)$$

where

$$qV_g' = qV_g - \phi_M + \Delta E_c + qV_p \quad (2.9)$$

and

$$V_p = \frac{qN_D}{2\epsilon}(d - d_s)^2 \quad (2.10)$$

where ϵ is the dielectric permittivity in the high-gap material (AlGaAs), V_g and V_c are the gate and channel potential relative to the source, ϕ_M is the Schottky barrier height, ΔE_c is the conduction band discontinuity, d is the width of the AlGaAs layer, and d_s is the spacer width. Here the Fermi level is assumed to be very close to the bottom of the potential well at the heterojunction.

With the assumptions stated earlier, Eq. (2.8) is taken to describe the electron sheet density along the channel from source ($x = 0$) to drain ($x = L$). The channel current j can then be expressed as

$$j = qn_s v = \frac{\epsilon}{d}[V'_g - V_c]\mu \frac{\partial V_c(x)}{\partial x} \quad (2.11)$$

which gives

$$V_c(x) = V'_g - \left[(V'_g - V_c(0))^2 - \frac{2djx}{\mu\epsilon} \right]^{\frac{1}{2}}, \quad (2.12)$$

where μ is the electron mobility. One can also include a source and drain resistance, R_s and R_d , in the drain voltage-current relation,

$$V_d = jR_d + V'_g - \left[(V'_g - jR_s)^2 - \frac{2djx}{\mu\epsilon} \right]^{\frac{1}{2}}. \quad (2.13)$$

The assumptions of the model can be considered valid only under low drain voltages, implying subsaturation. Under high drain voltages, the parallel field can be as large as the perpendicular field and the one-dimensional solution to Poisson's equation breaks down. Electrons are no longer confined in the lowest subband and in fact will occupy various subbands as well as the bulk. Consequently, transport in such a system includes both 2DEG and electrons in the 3D bulk, which in most cases cannot be adequately modeled by closed-form analytical expressions.

2.3 Numerical Models

For accurate results, the basic system of equations outlined in Section 2.1, namely the Boltzmann transport equation, Poisson's equation, and Schrödinger's equation, needs to be solved numerically over a two- or three-dimensional domain. A number of two-dimensional numerical models on HEMT have been developed [5],[6],[11],[12]. Transport is simulated by solving the

moment equations derived from the Boltzmann transport equation. The most common approach is to solve the first two moment equations along with Poisson's equation.

First moment equation, or continuity equation:

$$\frac{\partial n}{\partial t} = \frac{1}{q} \nabla \cdot \mathbf{j}_n + G_n - U_n \quad (2.14)$$

$$\frac{\partial p}{\partial t} = -\frac{1}{q} \nabla \cdot \mathbf{j}_p + G_p - U_p \quad (2.15)$$

Second moment equation, or current density equation:

$$\mathbf{j}_n = -qn\mu_n \nabla V + qD_n \nabla n \quad (2.16)$$

$$\mathbf{j}_p = -qp\mu_p \nabla V - qD_p \nabla p \quad (2.17)$$

Poisson's equation:

$$\nabla \cdot (\epsilon \nabla V) = q(n - p - N_D + N_A) \quad (2.18)$$

where V is the electrostatic potential, ϵ is the dielectric permittivity, q is the magnitude of the electronic charge, μ is the mobility, D is the diffusivity, \mathbf{j}_n and \mathbf{j}_p are the electron and hole current densities, G_n and G_p are the electron and hole generation rates, and U_n and U_p are the electron and hole recombination rates, respectively. Since the hole concentration in HEMT is much smaller than the electron concentration, the hole concentration and its current are usually ignored. Because of low impurity level in the conduction channel, generation and recombination are also ignored in most HEMT models.

Widiger [6] takes into account of electron heating by using hydrodynamic-like transport equations, which include two higher order moment equations in addition to the continuity equation and the current density equation.

$$\frac{\partial nE}{\partial t} = -\mathbf{j} \cdot \nabla V - nB - \nabla \cdot \mathbf{s} \quad (2.19)$$

$$\mathbf{s} = \mu_E n E \nabla V - \nabla(D_E n E) \quad (2.20)$$

where E is the average electron energy, \mathbf{s} is the energy flux, B is the energy-dissipation factor, μ_E is the flux mobility, and D_E is the flux diffusivity. Similar equations apply for both electrons in the bulk and those in the quantum well, with ∇ representing $(\partial/\partial x, \partial/\partial y)$ in the bulk and $\partial/\partial y$ in the quantum well respectively. Coefficients μ, D, μ_E, D_E , and B are all functions of the average energy E and are determined from experimental results and Monte Carlo simulations. Results of this study show that the hot-electron effects and the two-dimensional properties of Poisson's equation are significant.

Thermionic emission and electron tunneling across the heterojunction have been included [12] using a current density expression,

$$j_{\perp} = -q S_{\perp} \left[n(x_j^-) - n(x_j^+) \exp\left(\frac{-\Delta V_n}{kT}\right) \right] \gamma_n \quad (2.21)$$

where j_{\perp} denotes the current density normal to the heterojunction, S_{\perp} the interface velocity, $n(x_j^-)$ and $n(x_j^+)$ the electron density at AlGaAs side and the GaAs side of the junction, γ_n a factor taking into account of tunneling, and ΔV_n is the discontinuity in the electron band parameter given by,

$$\Delta V_n = \Delta\chi + kT \log \left[\frac{N_c(x_j^+)}{N_c(x_j^-)} \right] + kT \left[\frac{F_{1/2}(\eta_c)}{\exp(\eta_c)} \right] \quad (2.22)$$

where χ is the electron affinity and N_c the density of states. The last term in Eqn. (2.22) is a correction term to take the effect of Fermi-Dirac statistics into account.

An accurate numerical model requires an adequate knowledge of the physical device structure, the boundary conditions and the physical parameters such as mobility and diffusivity. Of particular importance is the

modeling of mobility since electrons in GaAs are known to have velocity overshoot under low electric field. Such velocity saturates when the electric field gets sufficiently large. It has been shown [23] that accurate description of the velocity-field characteristics is important in predicting device performance. In [6] transport parameters such as mobility and diffusivity are taken as functions of the average electron energy instead of functions of the electric field. Such energy dependencies are determined from Monte Carlo simulations with consideration of the major scattering mechanisms. Another non-ideal feature that needs to be taken into account is the surface defect states at the interface between the AlGaAs layer and the capping dielectric. These surface states act as traps to electrons and affect the performance of the device. However, it has been shown [5] that HEMT is less sensitive to surface traps than are some other devices such as the GaAs-gate-FET.

2.4 Monte Carlo Simulations

The Monte Carlo method is another popular technique to the solution of the Boltzmann equation, and thus is gaining ground as a powerful technique in device simulation in recent years [13], [14]. Instead of solving the transport problem in terms of macroscopic quantities such as current density, energy flux, mobility and diffusivity, the Monte Carlo method simulates the motion of microscopic particles in both real space and momentum space. These microscopic particles are treated as classical particles which undergo free flights in both real space and momentum space until scattering events occur. Because of the randomness of the scattering events, statistical fluctuations prevail in the distribution of the particles, but as the number of sample events increases the uncertainty in the statistical measurement decreases

and the resulting electron distribution becomes a solution to the Boltzmann transport equation.

For a uniform medium such as a pure semiconductor, it suffices to simulate only one particle based on the principle of ergodicity which states that the expectation value of an ensemble can be approximated by the expectation value of a single particle over a sufficiently long period of time. For a non-uniform material such as a heterostructure device, the principle of ergodicity fails and the simulation is performed over an ensemble of particles, typically of the order of 10,000. The strength of this approach lies in its ability to study transport phenomena at the microscopic level, revealing important time-dependent and space-dependent effects. In the numerical approach which solves macroscopic equations, problems exist in characterising fictitious quantities such as mobilities. Such problem is readily solved here as individual scattering mechanisms are taken into account for the transport of particles.

Wang and Hess [15] have studied the distribution of electron velocity at high fields using a three-dimensional Monte Carlo, neglecting the quantum effects. Two-dimensional effects have been investigated by Tomizawa et al. [16] in his Monte Carlo in which electrons in the quantum well are treated using two-dimensional scattering rates.

Works by Price [17, 18], Walukiewicz et al. [19], Yokoyama and Hess [20], and Ravaioli and Ferry [21] have included the quantum effects in their Monte Carlo. References [17], [18], [19], [21] employ a two-subband triangular well approximation for the quantum well, whereas reference [20] treats up to five subbands using a self-consistent calculation of the electronic states in the quantum well.

Chapter 3

Our Numerical Approach

3.1 Device Structure

The physical device structure in this HEMT model is represented by a two-dimensional geometry of the form shown in Fig. 3.1. Both the gate length and the impurity doping level in the AlGaAs layer are input parameters of the computer program and are to be specified by the user. On the two sides of the gate are two $0.5 \mu m$ regions separating the gate from the source and drain. Beneath the gate is a highly doped $Al_xGa_{1-x}As$ layer of width 50nm and aluminum mole fraction $x = 0.3$. A 10nm spacer region made of undoped AlGaAs lies between the highly doped AlGaAs layer and the GaAs layer. Such spacer layer is included to separate the free electrons in the GaAs channel from their donor impurities in AlGaAs reducing the scattering of electrons. The GaAs region consists of a quantum well of width 100nm and a bulk layer of width 300nm, noting that the two layers overlap each other as is shown in Fig. 3.1. The doping level of GaAs is $10^{14}cm^{-3}$. On the two sides are boundaries to two highly-doped GaAs regions, serving as ohmic contacts to the source and drain.

3.2 Transport

Transport in HEMT with hot electron effects is described by the following four moment equations derived from the Boltzmann transport equation [6],[23].

$$\frac{\partial n}{\partial t} = \frac{1}{q} \nabla \cdot \mathbf{j} + G \quad (3.1)$$

$$\mathbf{j} + \frac{\partial}{\partial t}(\tau_{HF}\mathbf{j}) = -q\mu n \nabla V + q \nabla(Dn) \quad (3.2)$$

$$\frac{\partial nE}{\partial t} = -\mathbf{j} \cdot \nabla V - nB - \nabla \cdot \mathbf{S} \quad (3.3)$$

$$\mathbf{S} + \frac{\partial}{\partial t}(\tau_{HF}\mathbf{S}) = \mu_E n E \nabla V - \nabla(D_E n E) \quad (3.4)$$

where n is the electron concentration, \mathbf{j} is the electron current density, q is the magnitude of the electronic charge, E is the average electron energy, \mathbf{S} is the energy flux, G is an electron redistribution term, and the various coefficients, μ , D , B , μ_E , D_E , and τ_{HF} , are the mobility, diffusivity, energy dissipation factor, flux mobility, flux diffusivity, and high energy frequency factor, respectively. The above four equations adequately describe transport in both the one-dimensional quantum well system and the two-dimensional bulk system, with ∇ representing $(\partial/\partial x, \partial/\partial y)$ in the bulk and $\partial/\partial y$ in the quantum well.

In our model, the recombination and generation of carriers in the unintentionally doped GaAs layer are assumed to be negligible. The generation-like term, G , in Eq. (3.1) is artificially included to redistribute the carrier concentration between the quantum well and the bulk in order to maintain a quasi-equilibrium between the two systems (see Section 3.3.)

The coefficients μ_E and D_E have been shown [6] to relate linearly with

μ and D , respectively, by assuming a Boltzmann distribution,

$$\mu_E = \alpha\mu \quad (3.5)$$

$$D_E = \alpha D \quad (3.6)$$

where

$$\alpha = \frac{\langle \tau E_i^2 \rangle}{\langle \tau E_i \rangle \langle E_i \rangle} \quad (3.7)$$

where τ is the energy relaxation time, E_i is the electronic energy, and the brackets in Eq. (3.7) refer to statistical averages over the entire sample. For a power-law scattering α has a constant value of

$$\alpha = \frac{2}{3}\left(p + \frac{5}{2}\right) \quad (3.8)$$

where the power-law scattering is defined as

$$\tau \propto E_i^p. \quad (3.9)$$

For polar optical phonons in GaAs, p has a value of 0.5 [6],[32].

Also terms in Eqs. (3.2) and (3.4) involving the high frequency parameter τ_{HF} can be ignored [6] since it is of the order of 0.1 ps whereas typical transient time is of the order of 10 ps. Substituting Eqs. (3.2) and (3.4) into Eqs. (3.1) and (3.3) respectively yields,

$$\frac{\partial n}{\partial t} = \nabla \cdot [-\mu n \nabla V + \nabla(Dn)] + G \quad (3.10)$$

and

$$\frac{\partial nE}{\partial t} = -\mathbf{j} \cdot \nabla V - nB + \nabla \cdot \alpha[-\mu n E \nabla V + \nabla(DnE)]. \quad (3.11)$$

The terms in Eqs. (3.10) and (3.11) involving μ correspond to transport of electrons and average energy under the influence of electric field, whereas the

terms involving D correspond to transport of electrons and average energy due to diffusion processes, respectively.

The transport equations are solved along with Poisson's equation given by

$$\frac{\partial^2 V}{\partial x^2} + \frac{\partial^2 V}{\partial y^2} = -\frac{q}{\epsilon}[N_D(x, y) - n(x, y)]. \quad (3.12)$$

where V is the electrostatic potential, ϵ is the dielectric permittivity, and N_D is the impurity doping level. The above equation applies to both the AlGaAs and GaAs regions with different dielectric constants and doping levels.

Eqs. (3.10), (3.11), and (3.12) constitute a complete system of equations for our transport model under both transient and steady state conditions. Here the three unknowns to be solved are n , E and V over the entire simulation domain.

3.3 The Quantum Well

Quantum effects are included in our model by means of a self-consistent solution of Schrödinger's equation and Poisson's equation. Schrödinger's equation describing the quantum well is of the form

$$-\frac{\hbar^2}{2m_x} \frac{d^2 \psi_i(x)}{dx^2} - qV(x, y) \psi_i(x) = E_i \psi_i(x) \quad (3.13)$$

where m_x is the electron conduction effective mass in the x-direction, ψ_i is the wavefunction corresponding to the eigenvalue E_i for the i -th subband, and $V(x, y)$ is the electrostatic potential. The boundary conditions are that the wavefunction vanishes at both infinities.

To model the quantum well, one possible approach is to define an artificial boundary across the GaAs region, separating the bulk system from the

quantized system. Electrons confined by such artificial boundary and the heterojunction are considered to be quantized and their motion is restricted to the y-direction; whereas electrons lying below the artificial boundary are considered as bulk carriers with no restriction to their motion. However, there are a number of shortcomings associated with such an approach. First, there is no definite rule to define the quantum well/bulk boundary. As the wavefunction spans over a relatively wide region in the quantum well, if the well width is taken too small, much of the wavefunction outside the boundary will be truncated and the quantum effect can be greatly distorted. On the other hand, if the well width is taken sufficiently large to include a significant portion of the wavefunction, the bulk electronic behavior will be neglected. Neither case is desirable from a device simulation standpoint. Second, the electron concentration over the quantum well/bulk boundary is in general discontinuous, which gives rise to large diffusion current across the boundary. This can cause erroneous results in the simulation. Third, at points where the electric field at the heterojunction is weak, the quantum well is too shallow to confine the electrons and the electrons at the heterojunction behave essentially as bulk carriers. Therefore, it is important that both the bulk and quantum characters of the electrons are considered, particularly at the heterojunction where the concentration of electrons is the highest.

We present here a different approach to this problem. In this approach, there is no artificial boundary separating the bulk GaAs from the quantum well. Instead, the two systems overlap each other. Furthermore, the quantum well is taken wide enough to include a significant portion of the wavefunction. Electrons in the bulk undergo transport in both the x- and

y-directions whereas electrons in the quantum well undergo transport in the y-direction only.

Since majority of the electrons in the quantum well reside in the lowest subband [22], in this thesis only transport in the lowest subband is considered. Electrons in higher subbands are treated as bulk electrons. In order to establish a relationship between the carrier concentration in the quantum well and that in the bulk, we assume that over the region where the quantum layer overlaps the bulk layer a quasi-equilibrium state is established between the relative electron distributions in the two systems, and the electron concentrations are given by,

$$N_{bulk} = N_C \exp\left(-\frac{E_1 - E_{Fn}}{kT}\right) \quad (3.14)$$

and

$$N_I = N_{I_C} \ln \left[1 + \exp\left(-\frac{E_0 - E_{Fn}}{kT}\right) \right] \quad (3.15)$$

where N_{bulk} and N_I are the electron sheet charge in the bulk and in the quantum well in their overlapping region, E_{Fn} is the quasi-Fermi energy, E_0 and E_1 are the minimum energies of the first two subbands, and N_C and N_{I_C} are the effective density of states of GaAs in the bulk and in the quantum well, respectively, and are given by,

$$N_C = 2 \left(\frac{mkT_L}{2\pi\hbar^2} \right)^{3/2} \quad (3.16)$$

and

$$N_{I_C} = 2 \left(\frac{mkT_L}{2\pi\hbar^2} \right) \quad (3.17)$$

where m is the effective mass of GaAs, k is Boltzmann's constant, and T_L is the lattice temperature.

We maintain such equilibrium between the quantum well and the bulk by means of a generation-like term G in Eq. (3.10); the term G re-distributes the electrons between the quantum layer and the bulk. The total electron sheet densities N_{bulk} and N_I in cm^{-2} for the bulk and the quantum well at each time step are calculated by integrating the electron concentrations over x in the overlapping region. Then the new equilibrium values for N_{bulk} and N_I are computed according to Eq. (3.14) and (3.15). The differences between the new and old values contribute to the generation/recombination terms as following

$$G_{bulk} = k * n_{bulk} * \frac{N_{bulk}^{new} - N_{bulk}^{old}}{N_{bulk}^{old}} \quad (3.18)$$

and

$$G_I = k * (N_I^{new} - N_I^{old}) \quad (3.19)$$

where k is a relaxation factor with value between 0 and 1, G_{bulk} is the bulk generation rate in cm^{-3} , G_I is the quantum well generation rate in cm^{-2} , and n_{bulk} is the bulk electron concentration in cm^{-3} . The relaxation factor serves to ensure smooth convergence of the result.

3.4 Solution of Schrödinger's Equation

The time-independent Schrödinger's equation is solved by the Rayleigh-Ritz method [24], [25]. Consider the following form of Schrödinger's equation

$$H\psi_i = E_i\psi_i \quad (3.20)$$

where H is the Hamiltonian operator, E_i is the eigenvalue, and ψ_i is the wavefunction. The eigenvalue can be evaluated based on variational principles

$$E_i = \min \frac{(H\psi, \psi)}{(\psi, \psi)} \quad (3.21)$$

where $(\psi, \psi_s) = 0; s = 1, 2, \dots, i-1$. The inner product of two wavefunctions is simply the integration of their product over the entire interval,

$$(\psi_1, \psi_2) \equiv \int_{-\infty}^{+\infty} \psi_1 \psi_2 dx \quad (3.22)$$

In practice, we express the desired wavefunctions in terms of some known wavefunctions f_i 's which are approximate solutions to Schrödinger's equation

$$\psi = c_1 f_1 + c_2 f_2 + \dots + c_M f_M \quad (3.23)$$

Expanding ψ in terms of the approximate wavefunctions, we have

$$(H\psi, \psi) = \left(H \sum_{m=1}^M c_m f_m, \sum_{n=1}^M c_n f_n \right) = \sum_{m,n} a_{mn} c_m c_n; \quad (3.24)$$

$$(\psi, \psi) = \left(\sum_{m=1}^M c_m f_m, \sum_{n=1}^M c_n f_n \right) = \sum_{m,n} b_{mn} c_m c_n, \quad (3.25)$$

where a_{mn} and b_{mn} are known constants given by,

$$a_{mn} = (H f_m, f_n); \quad (3.26)$$

$$b_{mn} = (f_m, f_n). \quad (3.27)$$

The wavefunction f_m when acted upon by the Hamiltonian operator gives

$$H f_m = -\frac{\hbar^2}{2m_x} \frac{d^2 f_m}{dx^2} + U(x) f_m(x) \quad (3.28)$$

where $U(x)$ is the potential energy, and by integration by parts

$$\int_{-\infty}^{+\infty} \frac{d^2 f_m}{dx^2} f_n dx = \frac{df_m}{dx} f_n \Big|_{-\infty}^{+\infty} - \int_{-\infty}^{+\infty} f'_m f'_n dx = - \int_{-\infty}^{+\infty} f'_m f'_n dx. \quad (3.29)$$

The first term in Eq. (3.29) vanishes because of the boundary conditions on the wavefunction

$$f_n(\infty) = f_n(-\infty) = f'_n(\infty) = f'_n(-\infty) = 0. \quad (3.30)$$

Therefore, a_{mn} can be expressed as

$$a_{mn} = \int_{-\infty}^{+\infty} \frac{\hbar^2}{m_x} f'_m f'_n + U(x) f_m f_n dx. \quad (3.31)$$

Similarly, b_{mn} can be expressed as

$$b_{mn} = \int_{-\infty}^{+\infty} f_m f_n dx. \quad (3.32)$$

Substituting Eqs. (3.24) and (3.25) into Eq. (3.21) we have

$$\sum_{m=1}^M \sum_{n=1}^M (a_{mn} - E_i b_{mn}) c_m c_n = 0. \quad (3.33)$$

Since both c_m and c_n are arbitrary in the above equation, the equality holds only if the determinant of the coefficients vanishes,

$$\begin{vmatrix} a_{11} - E_i b_{11} & a_{12} - E_i b_{12} & \cdots & a_{1M} - E_i b_{1M} \\ \vdots & \vdots & & \vdots \\ a_{M1} - E_i b_{M1} & a_{M2} - E_i b_{M2} & \cdots & a_{MM} - E_i b_{MM} \end{vmatrix} = 0. \quad (3.34)$$

The above equation when expanded into a polynomial of M -th degree gives M different roots of E_i . Eq. (3.34) cannot be solved analytically and iterative techniques such as the bisection method can be used. Variational theory shows that these energy values give the upper bound of the desired eigenvalues [25].

Once the eigenvalues E_i are found, the corresponding wavefunction can be easily evaluated by substituting E_i in and solving for the coefficients c_n from the equation

$$\sum_{m=1}^M (a_{mn} - E_i b_{mn}) c_m = 0, \quad (3.35)$$

where $n = 1, 2, \dots, M$. The wavefunctions obtained contains an arbitrary multiplicative constant and need to be normalized.

To obtain a set of functions on which the desired wavefunctions are expanded, we solve for the wavefunctions of a linearized potential well as

shown in Fig. 3.2. Schrödinger's equation describing such a potential well is given by

- In *AlGaAs*, $x \leq 0$,

$$\frac{d^2 f_i(x)}{dx^2} + \frac{2m_x}{\hbar^2} (E_i - \Delta E_c) f_i(x) = 0 \quad (3.36)$$

- In *GaAs*, $x \geq 0$,

$$\frac{d^2 f_i(x)}{dx^2} + \frac{2m_x}{\hbar^2} (E_i - q\mathcal{E}_s x) f_i(x) = 0 \quad (3.37)$$

where ΔE_c is the conduction band discontinuity, and \mathcal{E}_s is the electric field in the quantum well.

Solution of Eq. (3.36) is given by

$$f_i(x) = k_1 e^{\beta_i x} \quad (3.38)$$

where k_1 is a constant of integration and β_i is given by

$$\beta_i = \left(\frac{2m_x}{\hbar^2} (\Delta E_c - E_i) \right)^{\frac{1}{2}}. \quad (3.39)$$

To solve Eq. (3.37) we introduce a new function $u_I(\alpha_i) \equiv f_i(x)$ where

$$\alpha_i \equiv - \left(\frac{2m_x q \mathcal{E}_s}{\hbar^2} \right)^{\frac{1}{3}} \left(x - \frac{E_i}{q\mathcal{E}_s} \right). \quad (3.40)$$

The differential equation is simplified to the following

$$\frac{d^2 u_I(\alpha_i)}{d\alpha_i^2} - \alpha_i u_I(\alpha_i) = 0 \quad (3.41)$$

whose solution can be expressed in terms of the Airy function [24]

$$u_I(\alpha_i) = k_2 Ai(\alpha_i) \quad (3.42)$$

where k_2 is another constant of integration. The constants of integration k_1 and k_2 are determined by the boundary conditions and normalization of

the wavefunction. The boundary conditions are that both the function $f_i(x)$ and its first derivative are continuous at the heterojunction

$$k_1 e^{\beta \cdot 0} = k_2 Ai(\alpha_i(0)) \quad (3.43)$$

and

$$k_1 \left. \frac{d}{dx} e^{\beta x} \right|_{x=0} = k_2 \left. \frac{d}{dx} Ai(\alpha_i(x)) \right|_{x=0} \quad (3.44)$$

which gives

$$\gamma Ai'(\alpha_i(0)) - \beta_i Ai(\alpha_i(0)) = 0. \quad (3.45)$$

where

$$\gamma = \left(\frac{2m_x q \mathcal{E}_s}{\hbar^2} \right)^{\frac{1}{3}}. \quad (3.46)$$

Recall that the only variable in α_i is the electron energy E_i . Therefore, solving Eq. (3.45) gives us the allowed energy levels of the electron in the quantum well. Because of the implicit nature of Eq. (3.45), iterative methods are required to determine the energy eigenvalues.

Substituting Eq. (3.43) back into the original wavefunction equations, we have

- for $x \leq 0, (AlGaAs)$

$$f_i = C \cdot Ai(\alpha_i(0)) e^{\beta x} \quad (3.47)$$

- for $x \geq 0, (GaAs)$

$$f_i = C \cdot Ai(\alpha_i(x)) \quad (3.48)$$

where C is a normalization constant.

3.5 Boundary Conditions

The transport of electrons in the device is governed by three coupled, non-linear partial differential equations Eq. (3.10), (3.11), and (3.12) with three unknown variables n , E , and V . These equations are solved subject to the boundary conditions given in this section.

The electrostatic potential is continuous throughout the simulation domain (Fig. 3.3). We assume no interface state between the AlGaAs and GaAs layers and both the potential and its derivative are continuous at the heterojunction.

At the interface between the AlGaAs layer and the capping dielectric, $x = -d$ (see Fig. 3.1), the boundary condition for V is

$$\epsilon_{\text{AlGaAs}} \frac{\partial V}{\partial x} \Big|_{-d^+} = -qn_{ss} \quad (3.49)$$

where n_{ss} is the surface density of trapped charge at the interface. In our simulations, the value of n_{ss} is assumed to be constant along the entire interface between the AlGaAs layer and the capping dielectric. Such assumption is not expected to introduce significant errors. It has been shown [5] that the interface states in HEMT's do not affect the operation of the devices as much as they do in other FET devices since they are separated from the conducting channel by the insulating AlGaAs layer.

At the substrate boundary, $x = L_x$, we assume the electric field to be zero in the x-direction, and thus we have the boundary condition,

$$\frac{\partial V}{\partial x} \Big|_{L_x} = 0 \quad (3.50)$$

The electrostatic potential at the gate V_g is given by

$$V_g = V_{ga} + V_{bi} \quad (3.51)$$

where V_{ga} is the voltage applied across the gate and the substrate and V_{bi} is the built-in voltage given by

$$qV_{bi} = -\Phi_{MS} + \Delta E_c + E_F \quad (3.52)$$

where Φ_{MS} is the work function difference between metal and the semiconductor, ΔE_c is the conduction band discontinuity at the heterojunction, and E_F is the Fermi energy relative to the conduction band in the bulk GaAs (Fig. 3.3).

The electrostatic potential V and the electron concentration n in the source boundary are obtained by solving along with a one-dimensional Poisson's equation the following equation which assumes zero current density in the transverse direction [6]

$$q\mu n \frac{\partial V}{\partial x} - qD \frac{\partial n}{\partial x} = 0. \quad (3.53)$$

The boundary value for n on the drain side is the same as that in the source side, whereas that for V is taken as the source potential plus the difference between the drain and source voltages

$$V(x, L_y) = V(x, 0) + (V_d - V_s). \quad (3.54)$$

Assuming no leakage current from the device, the boundary conditions for n at the heterojunction and the bottom substrate boundary are given by,

$$j_t|_{x=0} = 0 \quad (3.55)$$

and

$$j_t|_{x=L_s} = 0. \quad (3.56)$$

where the transverse current density is given by

$$j_t = -q\mu n \frac{\partial V}{\partial x} + qD \frac{\partial n}{\partial x}. \quad (3.57)$$

Finally, we assume the average energy at all boundaries to attain equilibrium with the lattice, thus establishing the boundary condition for E

$$E = \frac{3}{2}kT_L \quad (3.58)$$

where T_L is the lattice temperature.

3.6 Numerical Stability Consideration

The numerical solution of the partial differential equations outlined in Section 3.2 requires iterative computation both in time and space. Numerical stability problems are often associated with such iterative techniques and careful consideration is needed to ensure smooth convergence of the results.

An explicit approach is commonly employed to solve the continuity equation

$$\frac{\partial n}{\partial t} = \frac{1}{q} \nabla \cdot \mathbf{J}, \quad (3.59)$$

which is discretized into the form

$$n^{k+1} = n^k + \Delta t \left(\frac{1}{q} \nabla \cdot \mathbf{J}^k \right). \quad (3.60)$$

The values of n and V at time k are plugged into the right-hand-side of Eq. (3.60) yielding the value of n at the next time step $k + 1$. This method is extremely straight forward requiring no complex matrix operation which means that the computation needed for each time step is minimal.

However, the major drawback of this approach is that excessively small time steps are required to guarantee numerical stability and to obtain accurate solutions. Specifically, it has been shown [26], [27] that the maximum time step one can use without having any stability problem is given by,

$$\Delta t < \min \left[\frac{\Delta x^2 \Delta y^2}{2D(\Delta x^2 + \Delta y^2)}, \frac{2D}{v_\infty^2} \right], \quad (3.61)$$

where Δx and Δy are the mesh spacings, D the diffusivity, and v_∞ the saturation velocity. When the maximum allowable time step is exceeded, a minor perturbation in the values of $n_{i,j}$ at mesh point (i,j) can result in a diverging solution.

The smallest mesh dimensions in this simulation are $2 \cdot 10^{-7}$ and $5 \cdot 10^{-6}$ cm, respectively. The diffusivity at low field is about $300 \text{ cm}^2/\text{s}$. Assuming the mesh spacing to be the limiting factor to the speed of the iterative process, the maximum time step one can use without causing numerical instability problem is

$$\Delta t < 6.6 \cdot 10^{-17} \text{ sec.}$$

which is of the order of 10^6 times smaller than the typical transient time of HEMT. This poses a serious problem for the convergence of the program.

In order to increase the time step to speed up the program, one has to increase the mesh spacing which in turn will sacrifice the accuracy of the result. Another approach to the solution of the continuity equation is to write the equation in an implicit form,

$$\frac{\partial n}{\partial t} = \frac{1}{2q} [\nabla \cdot \mathbf{J}^k + \nabla \cdot \mathbf{J}^{k+1}]. \quad (3.62)$$

where the superscript k represent time. The price to pay is complicated discretization and tedious solution. In this thesis, the implicit approach based on Eq. (3.62) is used.

3.7 Discretization Scheme

Transport of electrons in this model is described by Eqs. (3.10), (3.11) and (3.12). Note that Schrödinger's equation is solved assuming the electrons in the quantum well to be in quasi-equilibrium, and thus does not come into

the picture of transport directly. A finite-difference scheme is employed to solve the set of nonlinear second-order partial differential equations. Note that nonlinearity comes in because of the energy dependencies of various coefficients μ , D , and B , and the coupling of the variables n , E , and V .

The partial differential equations are written as a set of finite-difference equations at each point of a non-uniform rectangular mesh over the entire simulation domain. Since much of the action takes place in the quantum well, a high concentration of mesh points are placed along the channel near the heterojunction, resulting in very small mesh spacing in that region. These finite-difference equations are derived from truncated Taylor series with the assumption that the function involved and its derivatives are continuous and single-valued [26]. For a scalar quantity f defined at the major mesh points, its first derivatives are vector gradient components defined at the half-points as

$$\left. \frac{\partial f}{\partial x} \right|_{i+\frac{1}{2},j} = \frac{f_{i+1,j} - f_{i,j}}{x_{i+1} - x_i} \quad (3.63)$$

$$\left. \frac{\partial f}{\partial y} \right|_{i,j+\frac{1}{2}} = \frac{f_{i,j+1} - f_{i,j}}{y_{j+1} - y_j} \quad (3.64)$$

and its Laplacian, second derivative, is defined at the major mesh points as

$$\begin{aligned} \nabla^2 f \Big|_{i,j} &= \frac{1}{\frac{1}{2}(x_{i+1} - x_{i-1})} \left(\frac{f_{i+1,j} - f_{i,j}}{x_{i+1} - x_i} - \frac{f_{i,j} - f_{i-1,j}}{x_i - x_{i-1}} \right) \\ &+ \frac{1}{\frac{1}{2}(y_{j+1} - y_{j-1})} \left(\frac{f_{i,j+1} - f_{i,j}}{y_{j+1} - y_j} - \frac{f_{i,j} - f_{i,j-1}}{y_j - y_{j-1}} \right). \end{aligned} \quad (3.65)$$

In this thesis, the electrostatic potential V , the electron concentration n , and the average electron energy E are defined at the major mesh points; whereas first derivatives derived from these quantities such as the components of the electric field, current density and energy flux are defined at the half-points.

Poisson's equation, Eq. (3.12), is discretized into the form

$$\frac{2}{x_{i+1} - x_{i-1}} \left(\frac{V_{i+1,j} - V_{i,j}}{x_{i+1} - x_i} - \frac{V_{i,j} - V_{i-1,j}}{x_i - x_{i-1}} \right) + \frac{2}{y_{j+1} - y_{j-1}} \left(\frac{V_{i,j+1} - V_{i,j}}{y_{j+1} - y_j} - \frac{V_{i,j} - V_{i,j-1}}{y_j - y_{j-1}} \right) = -\frac{q}{\epsilon}(n_{i,j} - N_D) \quad (3.66)$$

The transport equations, Eq. (3.10) and (3.11), are discretized using the implicit form of Eq. (3.62)

$$n_{i,j}^{k+1} - \frac{\Delta t}{2q} \nabla \cdot \mathbf{J}_{i,j}^{k+1} = n_{i,j}^k + \frac{\Delta t}{2q} \nabla \cdot \mathbf{J}_{i,j}^k \quad (3.67)$$

and

$$(nE)_{i,j}^{k+1} + \frac{\Delta t}{2} \nabla \cdot \mathbf{S}_{i,j}^{k+1} = (nE)_{i,j}^k + \Delta t \left[-\mathbf{J} \cdot \nabla V - nB - \frac{1}{2} \nabla \cdot \mathbf{J} \right]_{i,j}^k \quad (3.68)$$

where the superscripts k denote discretization in time, subscripts i and j denote discretization in space, Δt is the time increment for each time step, \mathbf{J} is the current density, and \mathbf{S} is the energy flux. The components of the current density are

$$\mathbf{J}_{i+\frac{1}{2},j} = -q\mu_{i+\frac{1}{2},j} n_{i+\frac{1}{2},j} \frac{V_{i+1,j} - V_{i,j}}{x_{i+1} - x_i} + q \frac{D_{i+1,j}^t n_{i+1,j} - D_{i,j}^t n_{i,j}}{x_{i+1} - x_i} \quad (3.69)$$

in the x-direction, and

$$\mathbf{J}_{i,j+\frac{1}{2}} = -q\mu_{i,j+\frac{1}{2}} n_{i,j+\frac{1}{2}} \frac{V_{i,j+1} - V_{i,j}}{y_{j+1} - y_j} + q \frac{D_{i,j+1}^l n_{i,j+1} - D_{i,j}^l n_{i,j}}{y_{j+1} - y_j} \quad (3.70)$$

in the y-direction, where D^t and D^l are the transverse and longitudinal diffusivity respectively. The components of the energy flux are

$$\mathbf{S}_{i+\frac{1}{2},j} = -\alpha \left[\mu_{i+\frac{1}{2},j} (nE)_{i+\frac{1}{2},j} \frac{V_{i+1,j} - V_{i,j}}{x_{i+1} - x_i} + \frac{D_{i+1,j}^t (nE)_{i+1,j} - D_{i,j}^t (nE)_{i,j}}{x_{i+1} - x_i} \right] \quad (3.71)$$

in the x-direction, and

$$\mathbf{S}_{i,j+\frac{1}{2}} = -\alpha \left[\mu_{i,j+\frac{1}{2}}(nE)_{i,j+\frac{1}{2}} \frac{V_{i,j+1} - V_{i,j}}{y_{j+1} - y_j} + \frac{D_{i,j+1}^t(nE)_{i,j+1} - D_{i,j}^t(nE)_{i,j}}{y_{j+1} - y_j} \right] \quad (3.72)$$

in the y-direction. The term $\mathbf{J} \cdot \nabla V$ in Eq. (3.68) is [6]

$$\mathbf{J} \cdot \nabla V|_{ij} = \frac{V_{i+1j} - V_{ij}}{x_{i+1} - x_i} \mathbf{J}_{i+\frac{1}{2}j} + \frac{V_{ij} - V_{i-1j}}{x_i - x_{i-1}} \mathbf{J}_{i-\frac{1}{2}j} + \frac{V_{ij+1} - V_{ij}}{y_{j+1} - y_j} \mathbf{J}_{ij+\frac{1}{2}} + \frac{V_{ij} - V_{ij-1}}{y_j - y_{j-1}} \mathbf{J}_{ij-\frac{1}{2}} \quad (3.73)$$

taking into account of the contribution from current densities in all four directions.

A second-order partial differential equation

$$a \frac{\partial^2 \phi}{\partial x^2} + b \frac{\partial^2 \phi}{\partial x \partial y} + c \frac{\partial^2 \phi}{\partial y^2} + d \frac{\partial \phi}{\partial x} + e \frac{\partial \phi}{\partial y} + f \phi + g = 0 \quad (3.74)$$

is said to be elliptic [31] when $b^2 - 4ac > 0$. Careful inspection of Eqs. (3.66), (3.67), and (3.68) shows that these equations are indeed elliptic. Thus, a NAG library routine D03EBF for two-dimensional elliptic equations is employed to solve the above equations.

3.8 Transport Parameters

The transport parameters required in the transport equations Eqs. (3.67) and (3.68) are the transverse and longitudinal mobilities, μ_t and μ_l ; the transverse and longitudinal diffusion constants, D^t and D^l ; and the energy dissipation constant, B . These parameters and their energy dependencies have been provided by I. Kizilyalli and K. Hess¹ [11]. Linear interpolation is used to approximate the parameter values between the available data points.

¹I. Kizilyalli and K. Hess are with the Coordinated Science Laboratory, University of Illinois

Chapter 4

Results

In this chapter we present the results of our numerical simulation of HEMT which was performed under various biasing conditions at room temperature (300K). Such simulation has been performed on five different HEMT's with various device structures. The design parameters of these devices are tabulated in Table 4.1. Devices I, II and III have the same doping level of $5 \cdot 10^{17} \text{cm}^{-3}$ in the AlGaAs, but have different gate lengths 0.5, 0.7, and $1.0 \mu\text{m}$ respectively. Devices IV and V are simulated having the same gate length of $0.7 \mu\text{m}$ but different doping levels $2.5 \cdot 10^{17} \text{cm}^{-3}$ and $7.5 \cdot 10^{17} \text{cm}^{-3}$ respectively.

As boundary conditions, the electrostatic potential ψ and the electron concentration n at the source and drain boundaries are taken as fixed equilibrium values obtained by assuming zero net transverse current along both boundaries. These values are plotted in Figs. 4.1 and 4.2. It should be noted that the high peak of the electrostatic potential is due to the assumption of complete ionization of impurities in AlGaAs. Without the assumption the peak is expected to be somewhat lower.

Fig. 4.3 shows a typical wavefunction for the lowest subband of the quan-

tum well taken from a cross-section of the channel underneath the gate. Fig. 4.4 shows the corresponding eigenvalues E_0 and E_1 in relation to the potential profile, which have the values 46 and 69 meV respectively. These eigenvalues are of the same order of magnitude as those obtained from the triangular well approximation [20].

4.1 Drain Current Drain Voltage Characteristic

The variation of the drain current due to a change in the drain voltage provides important information on the operation of the device. Fig. 4.5 shows the drain current drain voltage characteristic of Device II under three different gate biasing conditions, where V_g equals 0.45 V, 0.5 V, and 0.7 V respectively. The slopes of the curves decrease as the drain voltage increases. There is no sharp transition from the linear region to the saturation region; nevertheless, one can easily identify the major device operating regions on the drain current drain voltage characteristic. With a gate bias of 0.45 V, the device has a linear I_D - V_D relationship when the drain voltage is under 0.5 V; the onset of saturation occurs at around 0.7 V. With a gate bias of 0.5 V, the linear section of the curve lies in the region where the drain voltage is less than 0.7 V; the onset of saturation occurs at around 1.2 V. In the case of a 0.7 V gate bias, the region under 0.7 V of drain voltage is approximately linear and the onset of saturation occurs at around 1.2 V.

To show the variations of the electrostatic potential, electron concentration, and current density along the channel, various plots are presented under two different sets of biasing conditions. In the first set, a gate voltage of 0.7 V and a drain voltage of 0.5 V are applied. In the second set, the gate bias is 0.7 V and the drain bias is 1.35 V. Figs. 4.6 and 4.7 show the electro-

static potentials in the device under the two drain biases 0.5 and 1.35 V. The dark region of the graphs due to densely populated mesh points is the quantum well. The AlGaAs region is located on top of the quantum well, whereas the source and drain are at the left and the right side boundaries respectively. Figs. 4.8 and 4.9 show the electron concentration in the bulk GaAs; Figs. 4.10 and 4.11 show the electron concentration in the quantum well. In the case of $V_d = 0.5$ V, the electron concentration in the channel is relatively uniform from source to drain, whereas in the case of $V_d = 1.35$ V, there is a sharp reduction in the electron concentration in the region underneath the drain end of the gate. This is the well-known pinch-off phenomenon of the field effect transistor. The transverse and longitudinal current densities are shown in Figs. 4.12 through 4.15. (A positive transverse current indicates a flow of electrons from the bulk GaAs to the heterojunction, whereas a positive longitudinal current indicates a flow of electrons from the drain to the source.) When a low drain voltage is applied, the longitudinal current is nearly uniform throughout the channel. This corresponds to the linear region of the $I_D \sim V_{DS}$ characteristic in which the change in the drain current is linearly proportional to the change in the drain voltage. When a high drain voltage is applied, the longitudinal current is no longer uniform, but decreases from the source along the channel and reaches a minimum at the pinch-off point. The pinch-off point acts as a bottleneck to the flow of current across the channel. As a result, the current is re-directed from the the heterojunction into the bulk, and the two-dimensional nature of electron transport becomes pronounced. This can be clearly seen from the large peak of the transverse current near the pinch-off point. As the flow of the current is limited by the electron concentration in the channel, the presence of a

pinch-off region prevents the drain current from increasing linearly with the drain voltage. Thus, the device reaches a saturation state.

4.2 Drain Current Gate Voltage Characteristic

We have studied the effects of the applied gate voltage on the electron transport in the GaAs channel by simulating the operation of Devices I-V under a fixed drain voltage of 1.0 V and various gate voltages ranging from 0.35 V to 1.35 V. Figs. 4.16 through 4.20 show the electron concentration for Device II under five different gate biasing conditions, where $V_g = 0.25, 0.5, 0.75, 1.0,$ and 1.25 V, respectively. The electron concentration in the conduction channel under the gate increases with the gate voltage as expected. The pinch-off phenomenon, as indicated by the valley in Fig. 4.16, is pronounced in the case of the 0.25 V gate bias. This is because the drain voltage is much higher than the gate voltage. Electrons in the channel are largely drawn toward the drain contact, resulting in a slightly depleted region underneath the gate, which is the pinch-off point. As higher gate voltages are applied, the pinch-off point disappears, as clearly demonstrated in Figures 4.17 through 4.20.

The terminal currents at the source and at the drain are obtained by integrating the longitudinal current density along the source and drain side boundaries, respectively. The steady state current is taken as the asymptotic value the drain and source terminal currents converge to over a sufficiently long period of time, typically of the order of 2 to 10 ps, depending on the initial state of the device. The transient drain and source currents, $i_s(t)$ and $i_d(t)$, for Device II under a gate voltage of 0.5 V are shown in Fig. 4.21. The resulting drain current-gate voltage ($I_D \sim V_G$) characteristics for De-

vices I-V are given in Fig. 4.22. For a fixed gate voltage, the drain current increases with decreasing channel lengths (Devices I, II and III). This is due to the fact that a shorter device has a lower overall channel resistance than that of a longer device. The drain current is also found to increase with increasing impurity doping concentrations in AlGaAs (Devices IV, II and V). Such increase is caused by a higher electron density in the conduction channel.

We also calculate the total charge in the device by integrating over the entire GaAs region the sum of the bulk and the quantum well electron densities

$$Q = \int_0^{L_y} \int_0^{L_x} q \cdot n dx dy. \quad (4.1)$$

Fig. 4.23 shows the relationship between the total charge in the GaAs layer (the quantum well and the bulk) and the applied gate voltage. The total charge in GaAs increases with increasing channel lengths (Devices I, II and III) and with increasing impurity doping levels in AlGaAs (Devices IV, II and V). The former result agrees with the general consideration that the longer the channel length the larger the volume of the device and thus the more is the charge in the GaAs layer. The latter result is due to the fact that variation in the concentration of impurity doping in AlGaAs causes variation in the electric field built up at the heterojunction and thus the amount of charge induced in the GaAs channel.

Based on the above results, we obtain values of the transconductance, the gate capacitance, and the unity-gain frequency according to the following formulae:

$$g_m = \frac{\partial I_d}{\partial V_g} \quad (4.2)$$

$$C_g = \frac{\partial Q}{\partial V_g} \quad (4.3)$$

and

$$f_T = \frac{1}{2\pi} \frac{g_m}{C_g}. \quad (4.4)$$

The transconductance values for the five devices simulated under various drain bias conditions are shown in Fig. 4.24. The graphs show a general pattern in which the transconductance increases with the gate voltage at low gate bias; however, as the gate bias is raised further, the transconductance levels off and then starts to decrease. Degradation of the transconductance under high gate voltages has been reported [11],[12] and has been a main interest of research. Similar patterns are observed in the plots of the gate capacitance (Fig. 4.25) and the unity-gain frequency (Fig. 4.26). One reason for the drop of the transconductance and the gate capacitance as the drain voltage is increased is that the electron concentration in the channel is limited by the supply of electrons at the source boundary, which can be clearly seen from Fig. 4.20. As a result, the electron concentration and thus the current density in the channel do not increase proportionally with the drain voltage. Other causes for the degradation of the transconductance has been suggested [5] such as the accumulation of electrons in the AlGaAs layer. The transport of electrons in AlGaAs, however, has not been included in our HEMT model; thus, the effects of such parallel conduction in AlGaAs cannot be concluded from our results. For Device II, the maximum transconductance obtained is 579.2 mS/mm at a gate bias of about 0.625 V. The gate capacitance at such gate bias is 19.28 pF/cm and the resulting unity-gain frequency is 47.8 GHz.

4.3 Effects of the Gate Length

The effects of the gate length can be studied from the $I_D \sim I_G$ characteristics of Devices I, II and III (Fig. 4.22) which have gate lengths of 0.5, 0.7 and 1.0 μm respectively. The transconductance as a function of the gate length is plotted in Fig. 4.27. A reduction of the gate length results in an increase of the drain current. Similar results are obtained in [33] although the values of the currents are different owing to different biasing conditions. This increase in drain current is partly due to a shift in the threshold voltage. By extrapolating the drain current gate voltage characteristics (Fig. 4.22) to the horizontal axis where $I_d = 0$ A/cm, the threshold voltages for Devices I, II, and III are found to be -0.44, -0.17, and -0.15 V respectively. Thus, Devices I, II and III are all depletion mode (normally-on) devices. In order to obtain an enhancement mode (normally-off) device, one can modify the device structure such as reducing the AlGaAs thickness. The unity gain frequencies for Devices I, II, and III are calculated to be 61.44, 47.8 and 38.9 GHz respectively at a drain bias of 0.875 V. Thus, the shorter the gate length the faster the switching speed the device can be operated on.

4.4 Effects of Doping

The effects of doping can be studied from the $I_D \sim V_G$ characteristics (Fig. 4.22) of Devices IV, II and V which have AlGaAs doping levels of $2.5 \cdot 10^{17}$, $5 \cdot 10^{17}$ and $7.5 \cdot 10^{17} cm^{-3}$, respectively. The transconductance as a function of the doping level is plotted in Fig. 4.28. An increase in the doping level gives rise to a larger drain current because there is a higher electron concentration in the channel. The transconductance values for De-

vices IV, II and V at a gate bias of 0.625 V are calculated to be 292.4, 597.2 and 664.4 mS/mm respectively. The corresponding gate capacitances are 9.21, 19.28 and 19.44 pF/cm, whereas the unity-gain frequencies for these devices at the same gate bias are found to be 50.54, 47.8 and 54.39 GHz respectively.

Chapter 5

Discussion and Conclusion

A two-dimensional numerical model for the High Electron Mobility Transistor has been developed with consideration of quantization in the heterojunction. The pinch-off phenomenon and the two-dimensional nature of electron transport have been demonstrated. A maximum transconductance of 531.2 mS/mm for a HEMT with gate length of 0.5 μm and a doping level of $5 \cdot 10^{17} \text{cm}^{-3}$ has been obtained, which has corresponding gate capacitance and unity-gain frequency of 13.8 pF/cm and 61.5 GHz respectively. The effects of the gate length and the impurity doping level in the AlGaAs have been investigated. It has been found that a reduction in the gate length gives rise to a decrease of the threshold voltage. Such shift in the threshold voltage causes more current to flow in the channel under the same bias conditions. An increase in the impurity doping level in the AlGaAs also affects the amount of current in the channel. The higher the doping level the higher is the density of free electrons in the device. Thus, a larger drain current is obtained. However such increase in drain current is expected to level off as the impurity doping level is further raised owing to incomplete ionization of these dopants and accumulation of electrons in the AlGaAs layer.

The values of the transconductance and the unity-gain frequencies obtained from these HEMT simulations are somewhat larger than reported values [11], [12],[33]. A number of factors may have contributed to these discrepancies. First, the assumed values for the electron concentration at the side boundaries may be larger than the actual values giving rise to an overestimation of the channel current. Second, we have assumed an ideal situation for the source and drain contact behavior in which the electron concentration is at the equilibrium value under all biasing condition. This obviously introduces some error in the simulation and contributes to an increase in the transconductance. An improvement on the modeling of the contacts requires further study on the the physics of the material. However, the HEMT model developed can be easily modified to include a more accurately described contact behavior. Thirdly, we have not been able to obtain the amount of electron heating as reported in [11], [33]. Fig. 4.29 plots the typical average energy values obtained in our simulations. In fact, in most cases in which a sufficiently large gate voltage is applied the amount of electron heating is found to be negligible. This gives rise to extremely high values of mobility throughout the device. Thus, the resulting current is overestimated. Further study on the hot electron problem is necessary in order to determine the role of electron heating in the operation of HEMT.

Future works on the numerical modeling of HEMT can be done in the following areas: First, electron conduction in the AlGaAs layer can be included with consideration of the tunneling current through the heterojunction and the leakage current through the gate Schottky barrier. The mobility model in the AlGaAs should take into account of the low-field mobility and the saturation velocity. Second, higher subbands in the quantum well can be

simulated. However, a scheme for coupling the electron transport in multiple subbands is not a trivial problem and may require elaborate theoretical analysis. Third, the role of interface states in HEMT can be studied.

Device	Gate Length (μm)	Channel Length (μm)	AlGaAs Thickness <i>nm</i>	AlGaAs Doping (cm^{-3})	GaAs Doping (cm^{-3})	Temp. (K)
I	0.5	1.5	600	$5.0 \cdot 10^{17}$	10^{14}	300
II	0.7	1.7	600	$5.0 \cdot 10^{17}$	10^{14}	300
III	1.0	2.0	600	$5.0 \cdot 10^{17}$	10^{14}	300
IV	0.7	1.7	600	$2.5 \cdot 10^{17}$	10^{14}	300
V	0.7	1.7	600	$7.5 \cdot 10^{17}$	10^{14}	300

Table 4.1: Devices Simulated

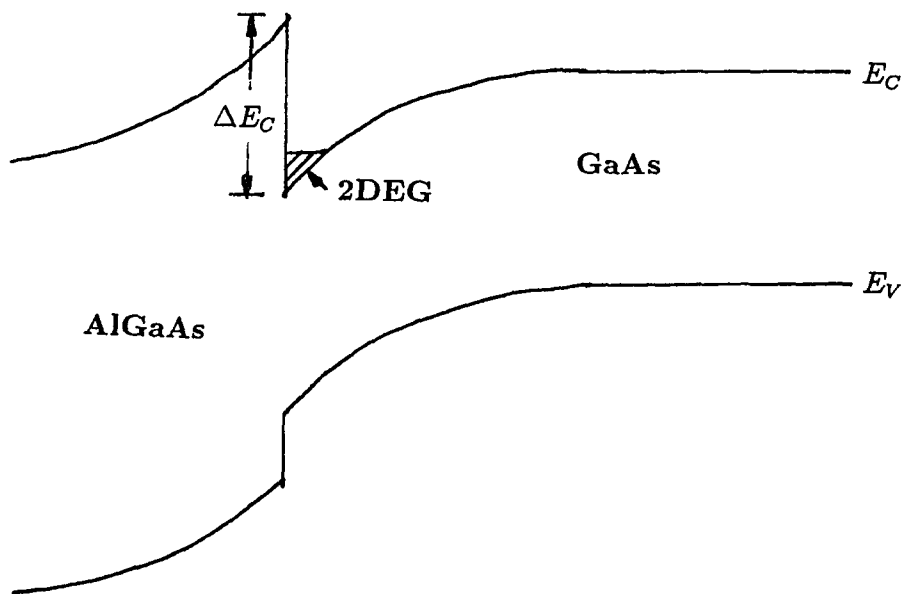


Figure 1.1: Formation of the 2DEG in GaAs

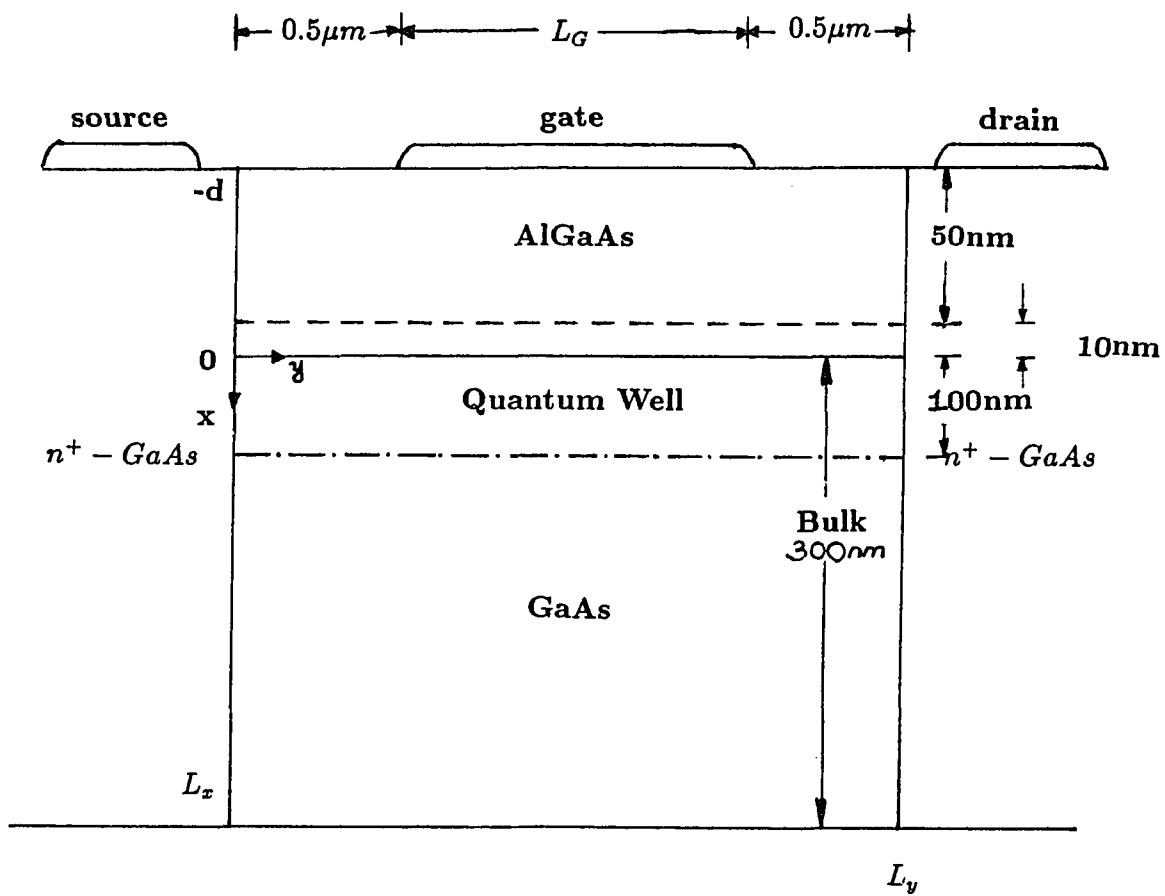


Figure 3.1: Device structure

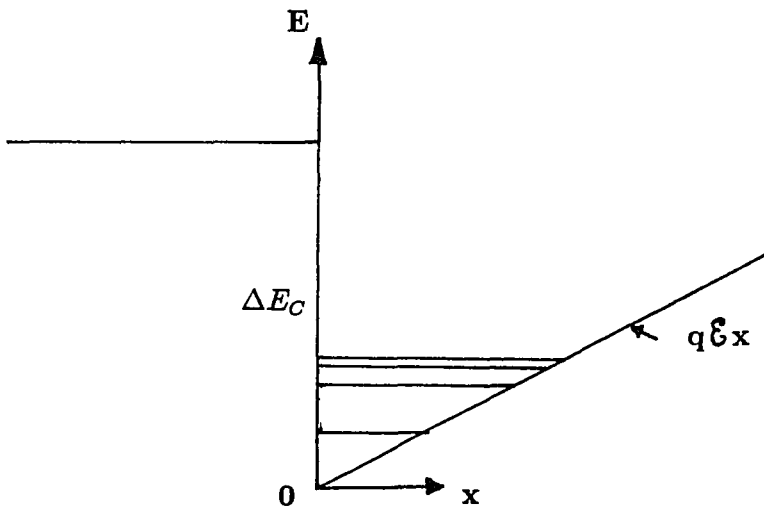


Figure 3.2: Linearized potential well

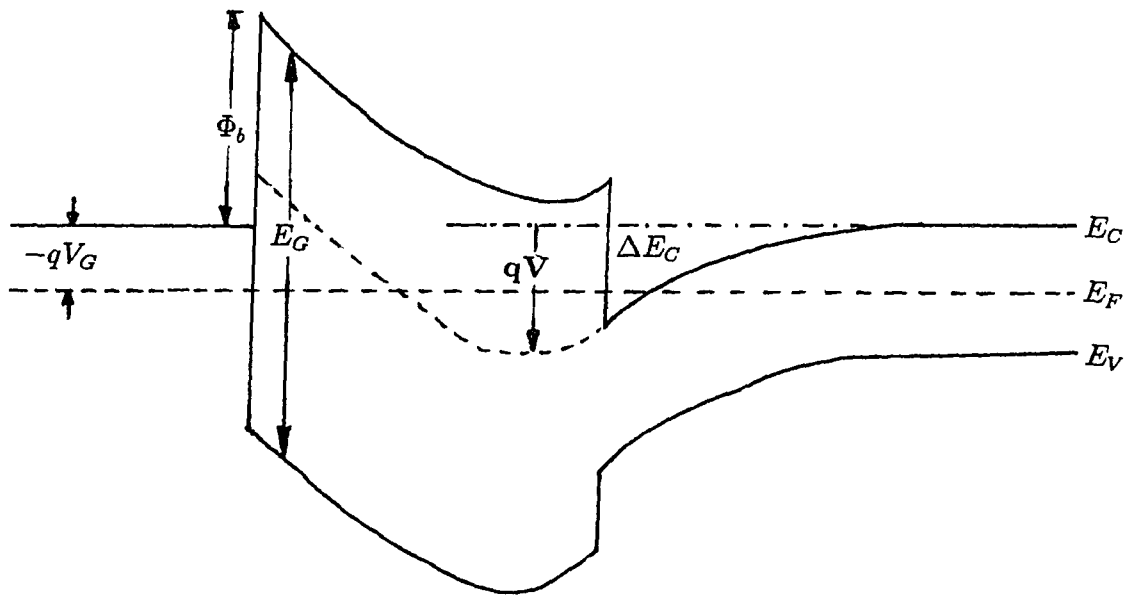


Figure 3.3: Electrostatic potential

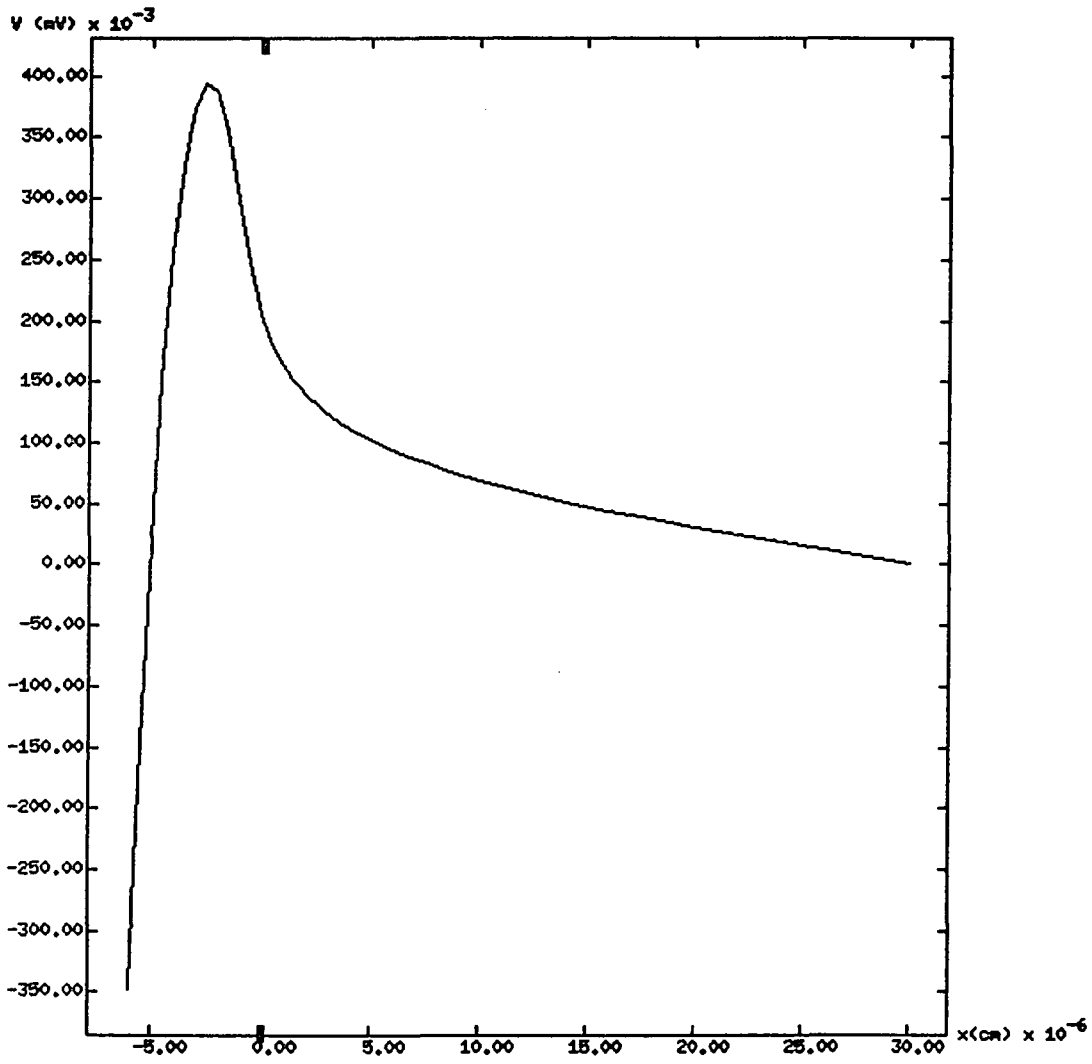


Figure 4.1: Electrostatic potential along the source boundary

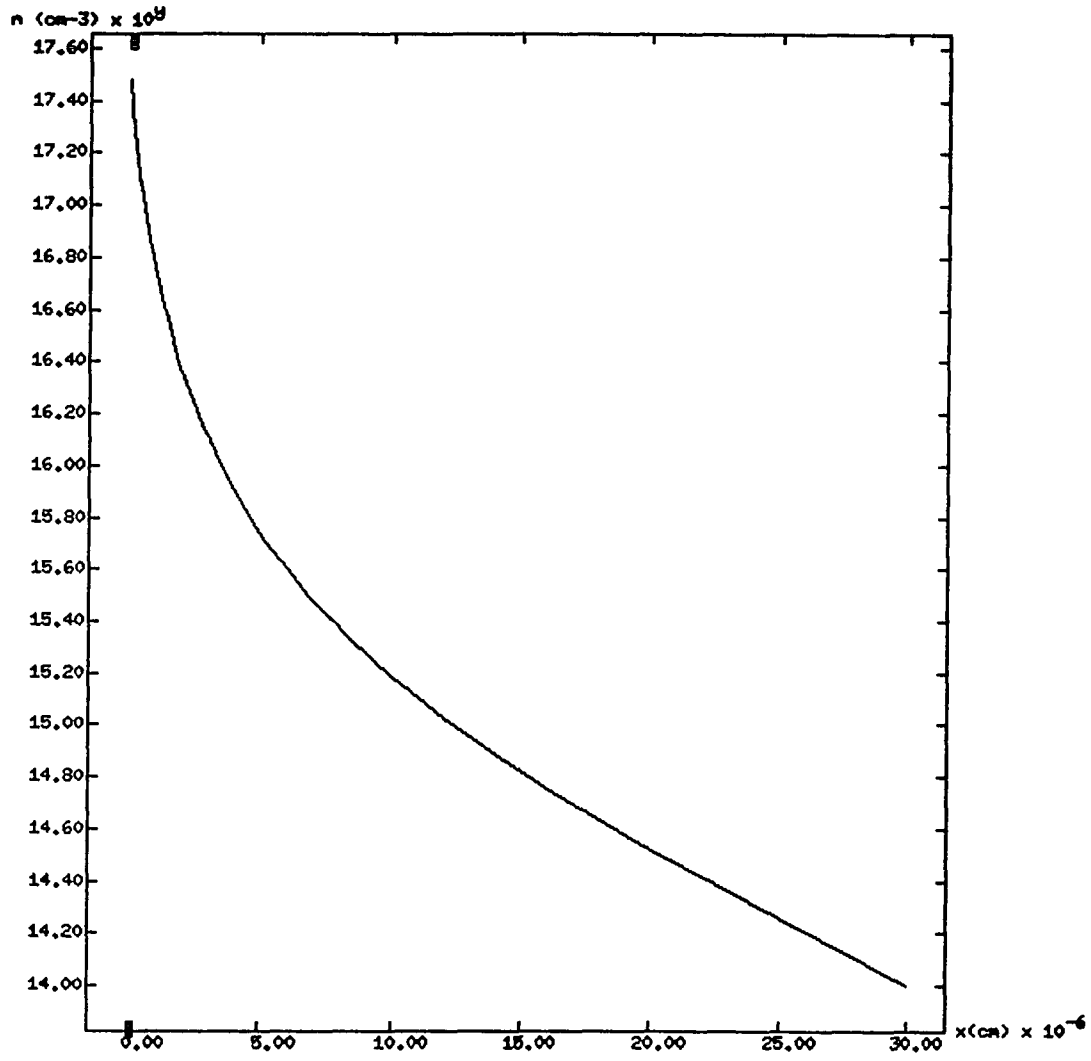


Figure 4.2: Electron concentration along the source boundary

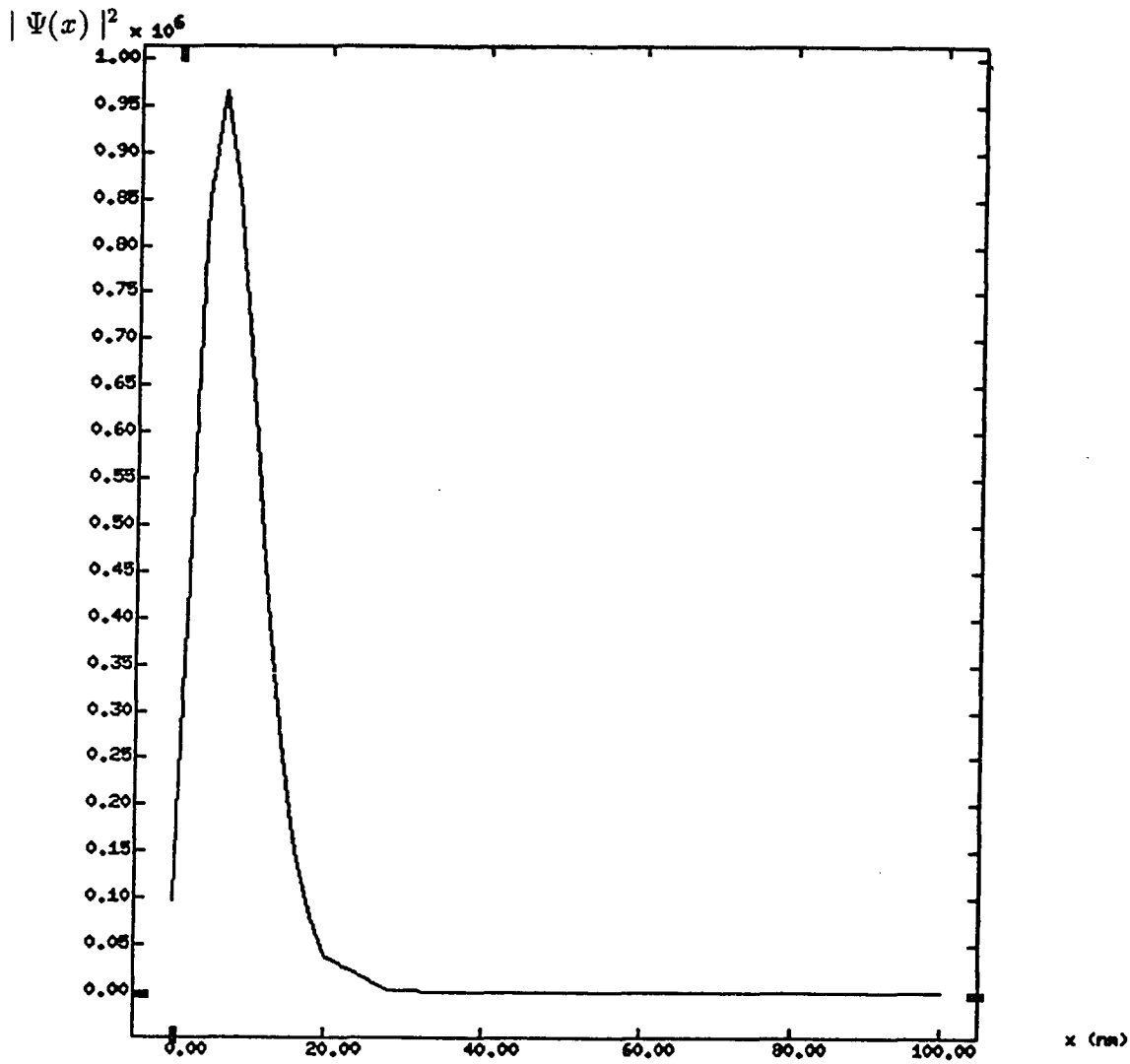


Figure 4.3: A typical wavefunction taken at a cross-section of the conducting channel

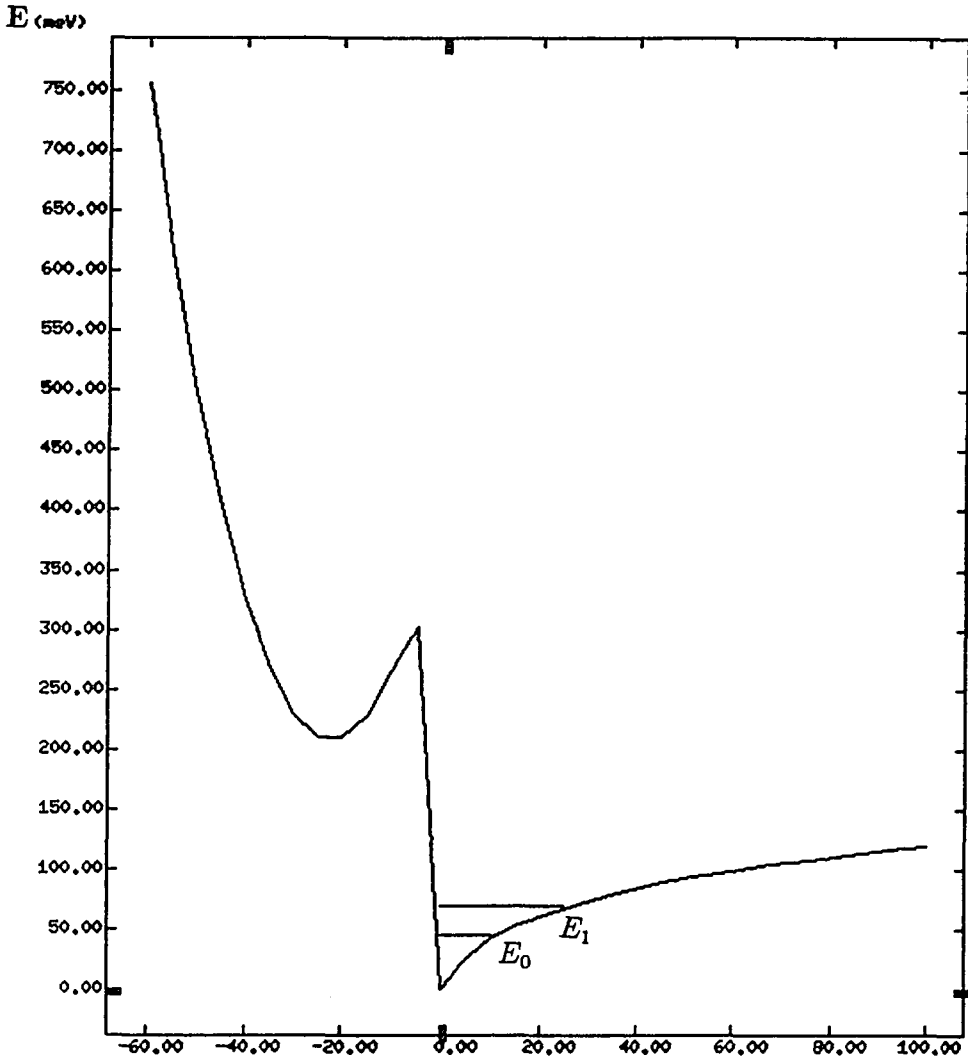


Figure 4.4: Energy subbands in the quantum well

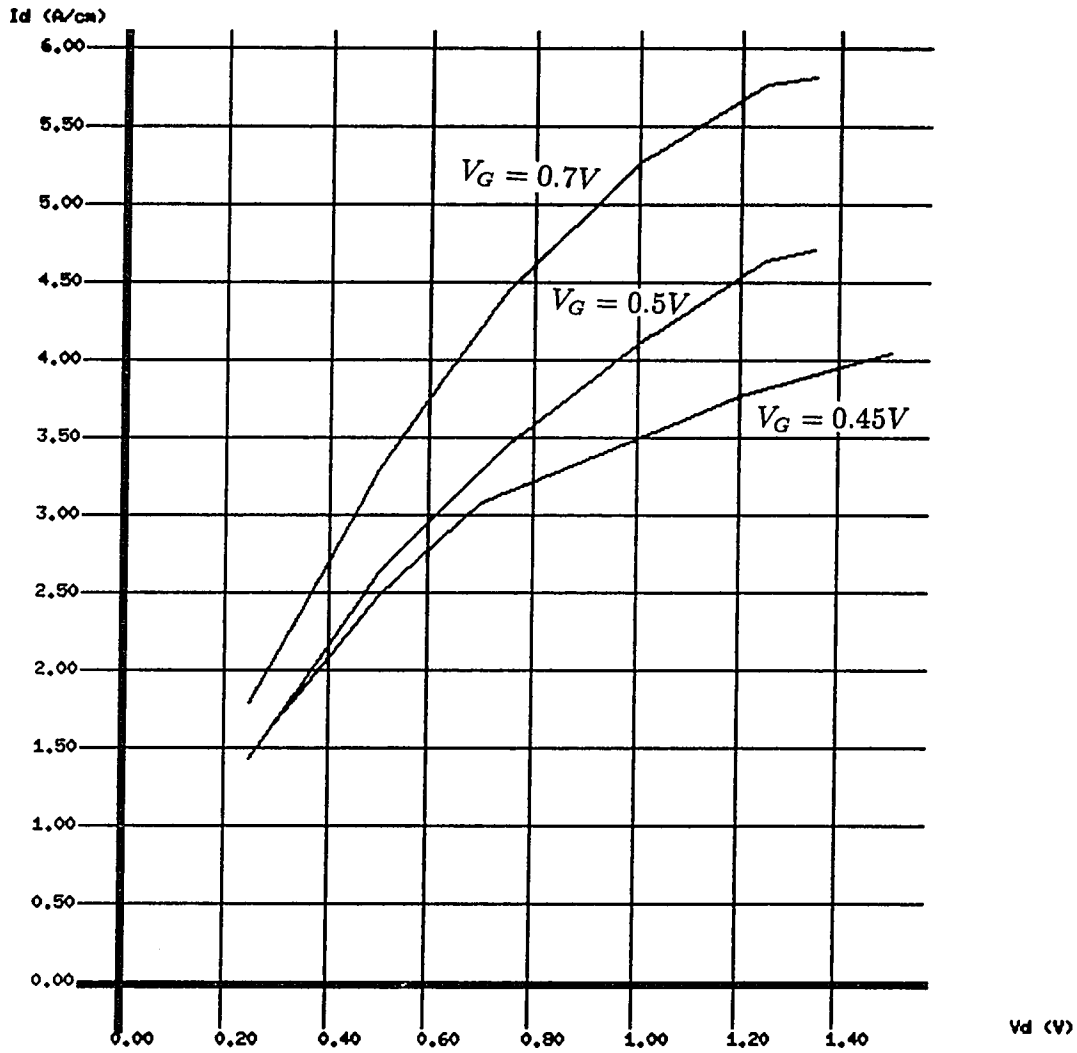


Figure 4.5: Drain current drain voltage characteristics for Device II

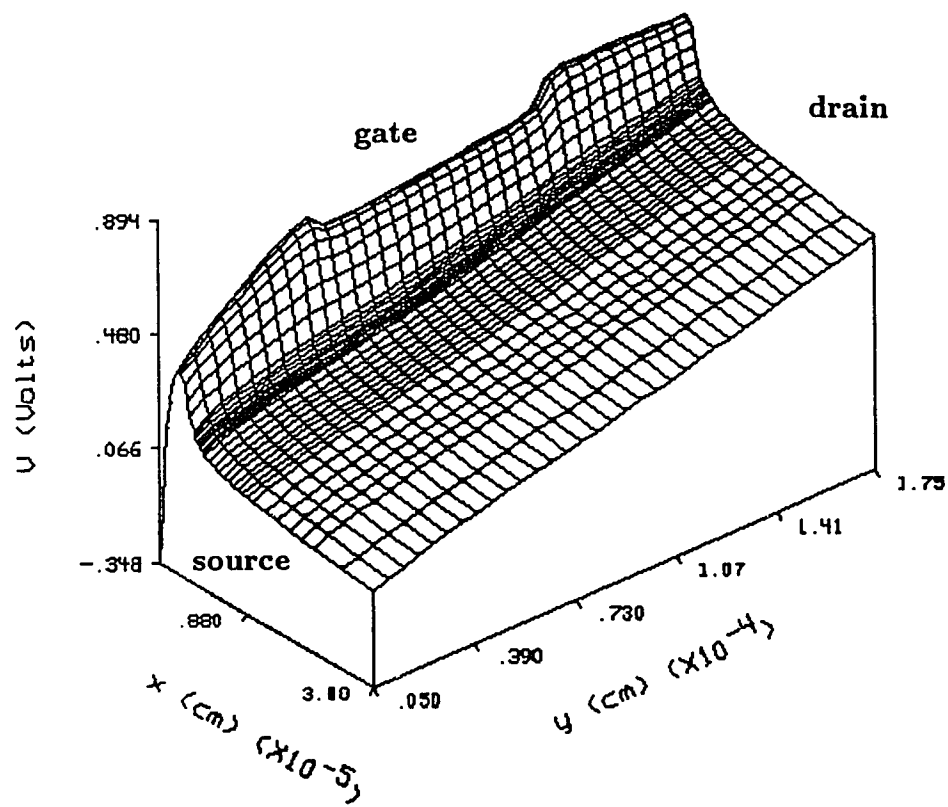


Figure 4.6: Electrostatic potential with a gate voltage of 0.7V and a drain voltage of 0.5V

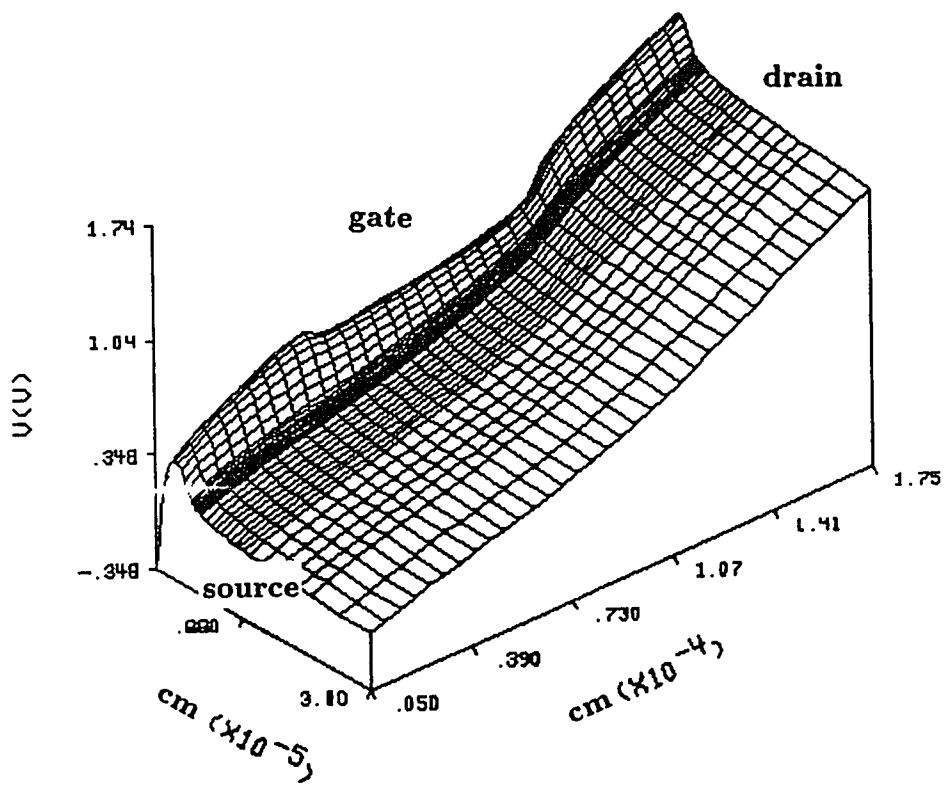


Figure 4.7: Electrostatic potential with a gate voltage of 0.7V and a drain voltage of 1.35V

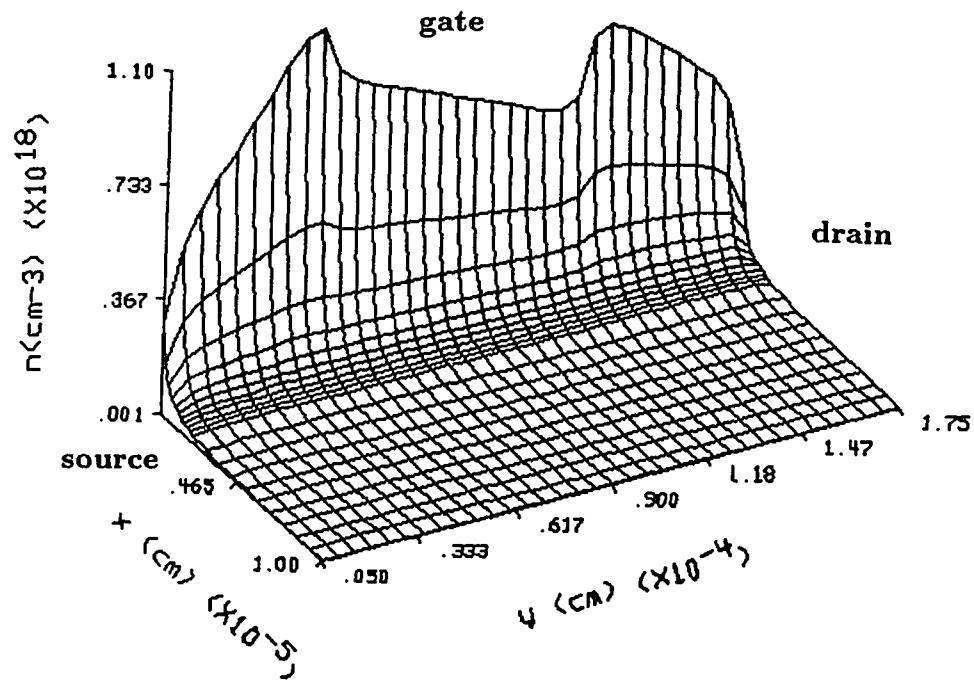


Figure 4.8: Electron concentration in the bulk with a gate voltage of 0.7V and a drain voltage of 0.5V

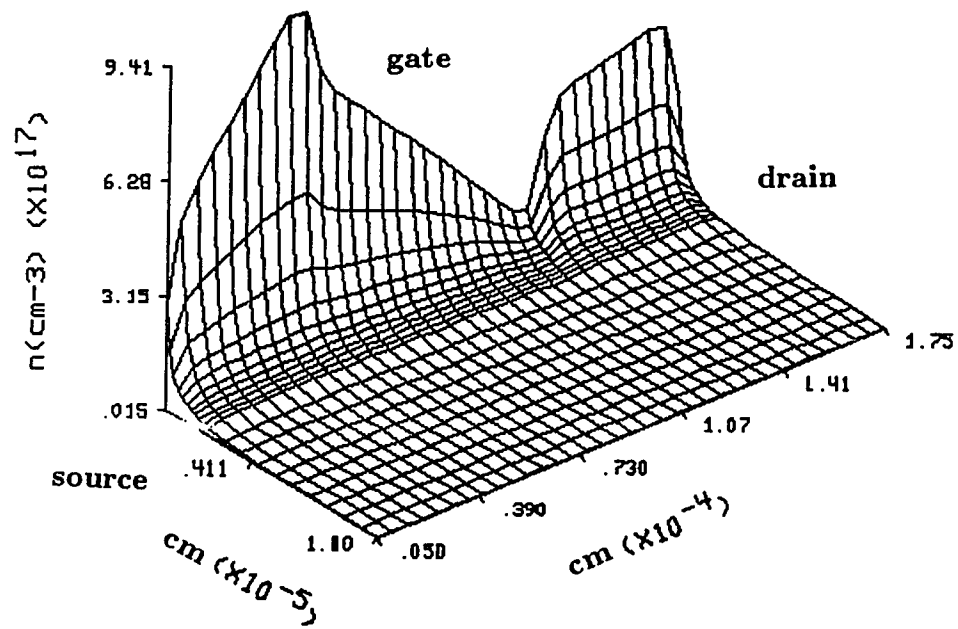


Figure 4.9: Electron concentration in the bulk with a gate voltage of 0.7V and a drain voltage of 1.35V

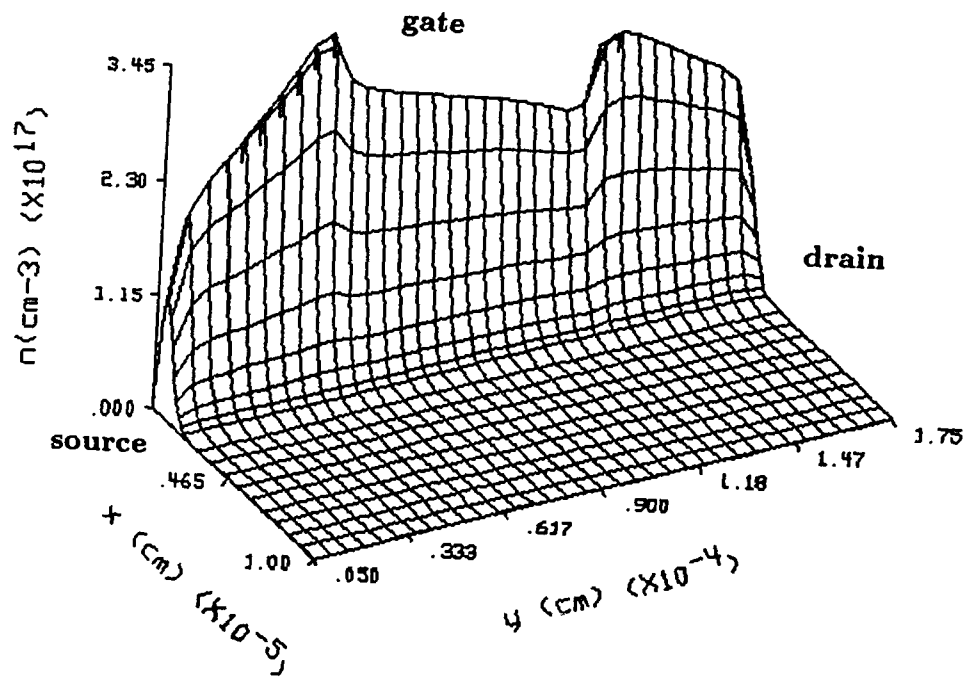


Figure 4.10: Electron concentration in the quantum well with a gate voltage of 0.7V and a drain voltage of 0.5V

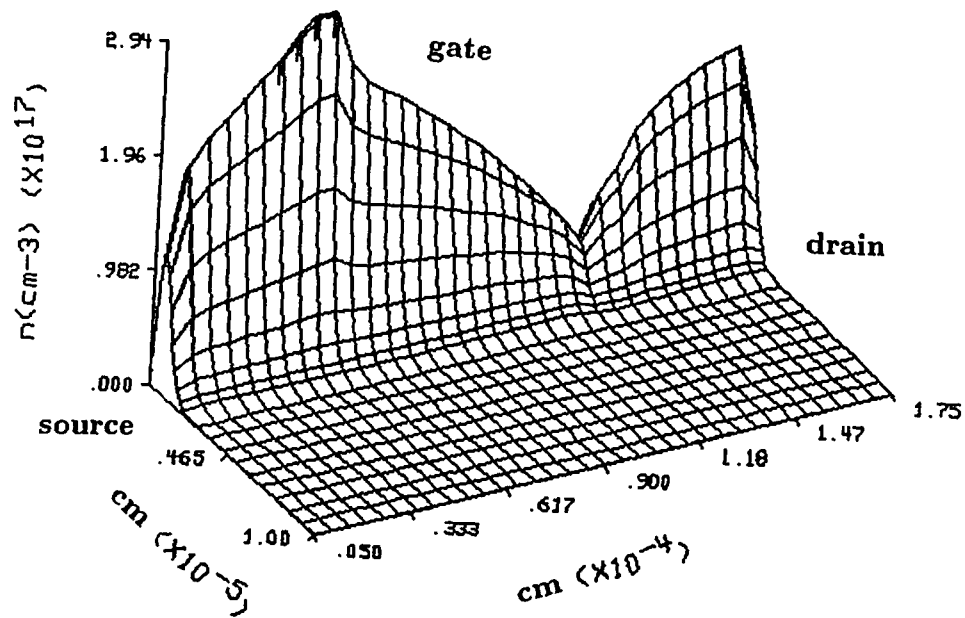


Figure 4.11: Electron concentration in the quantum well with a gate voltage of 0.7V and a drain voltage of 1.35V

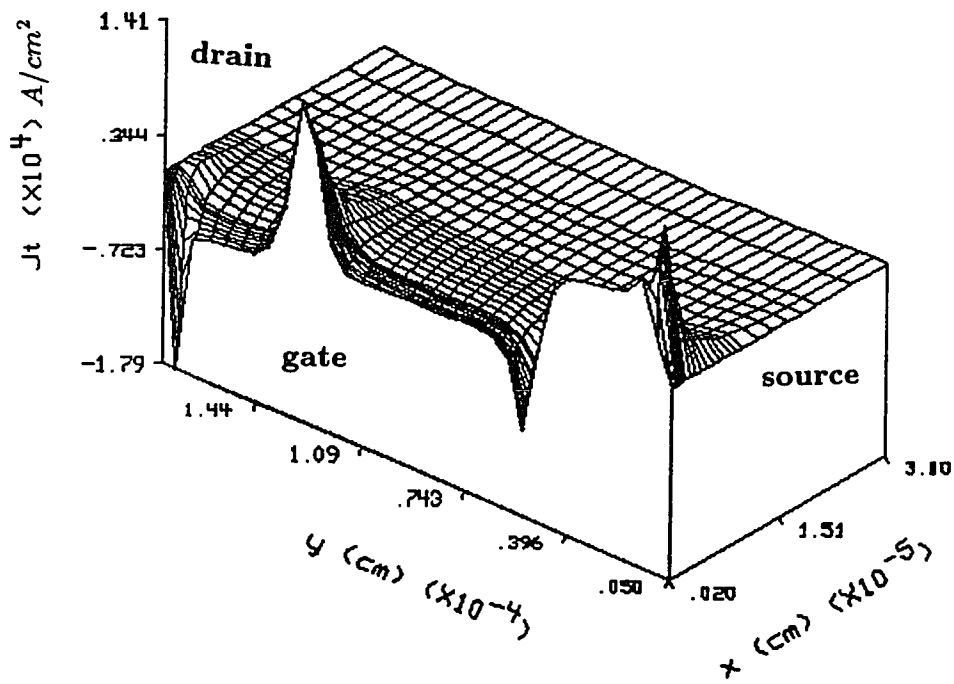


Figure 4.12: Transverse current density with a gate voltage of 0.7V and a drain voltage of 0.5V

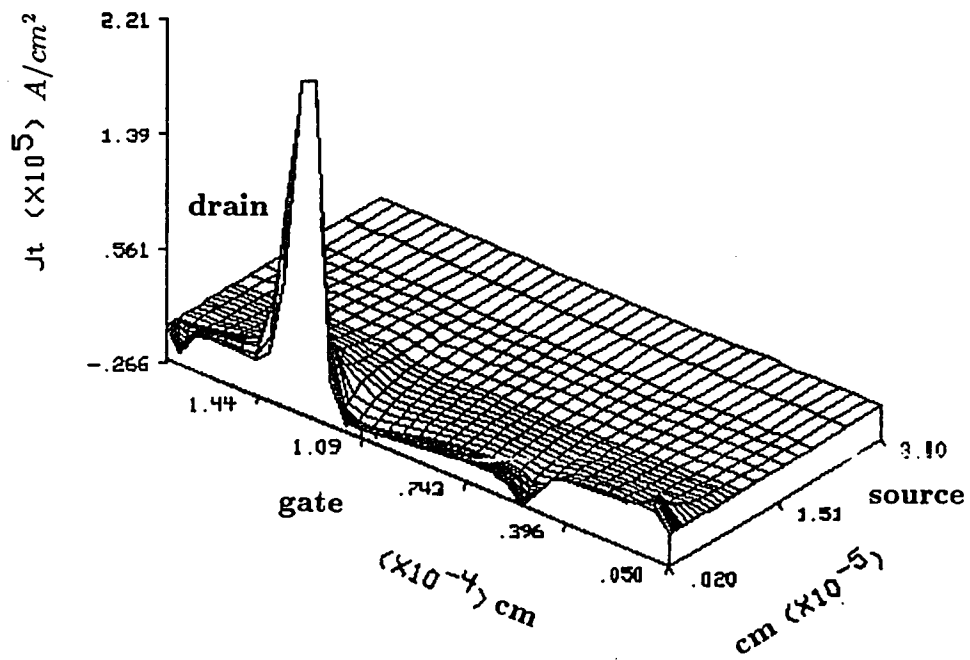


Figure 4.13: Transverse current density with a gate voltage of 0.7V and a drain voltage of 1.35V

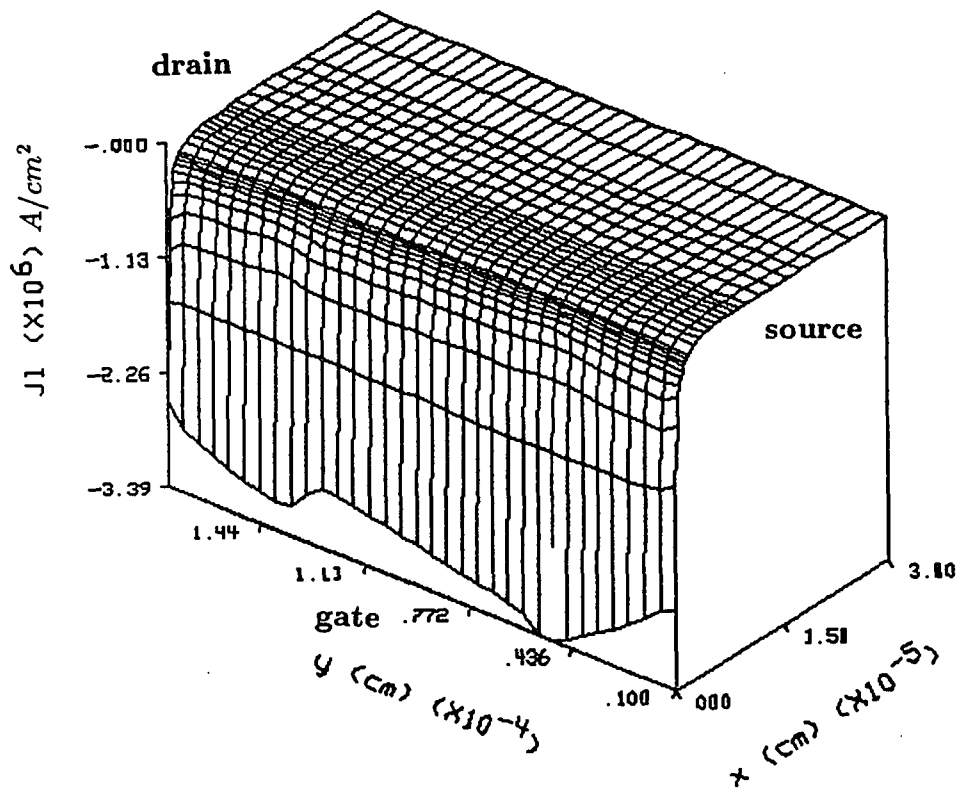


Figure 4.14: Longitudinal current density with a gate voltage of 0.7V and a drain voltage of 0.5V

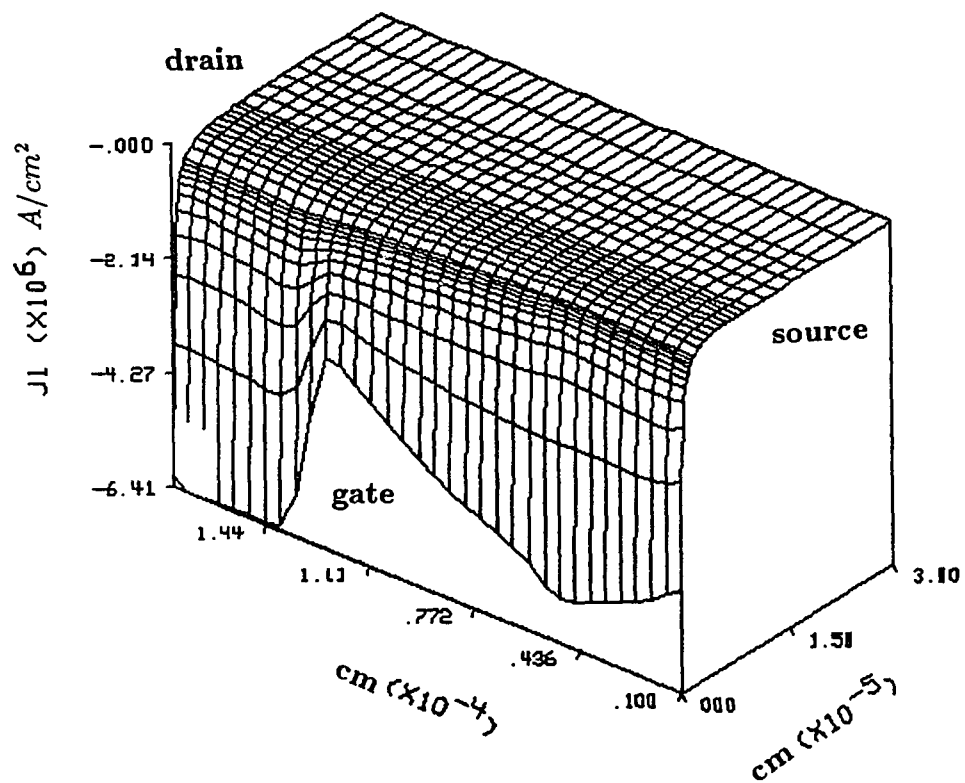


Figure 4.15: Longitudinal current density with a gate voltage of 0.7V and a drain voltage of 1.35V

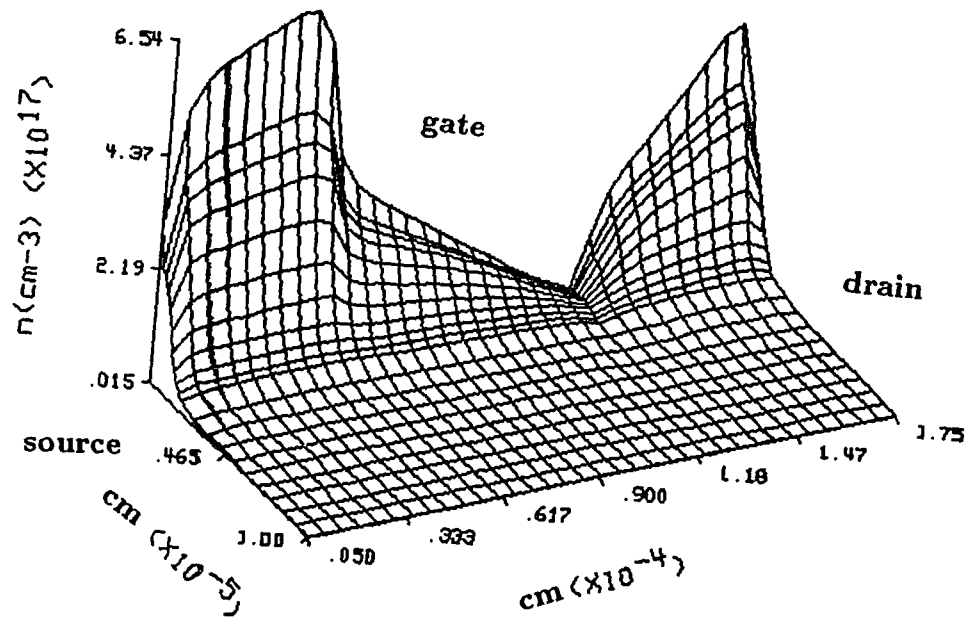


Figure 4.16: Total electron concentration in Device II with a gate voltage of 0.25V and a drain voltage of 0.9V

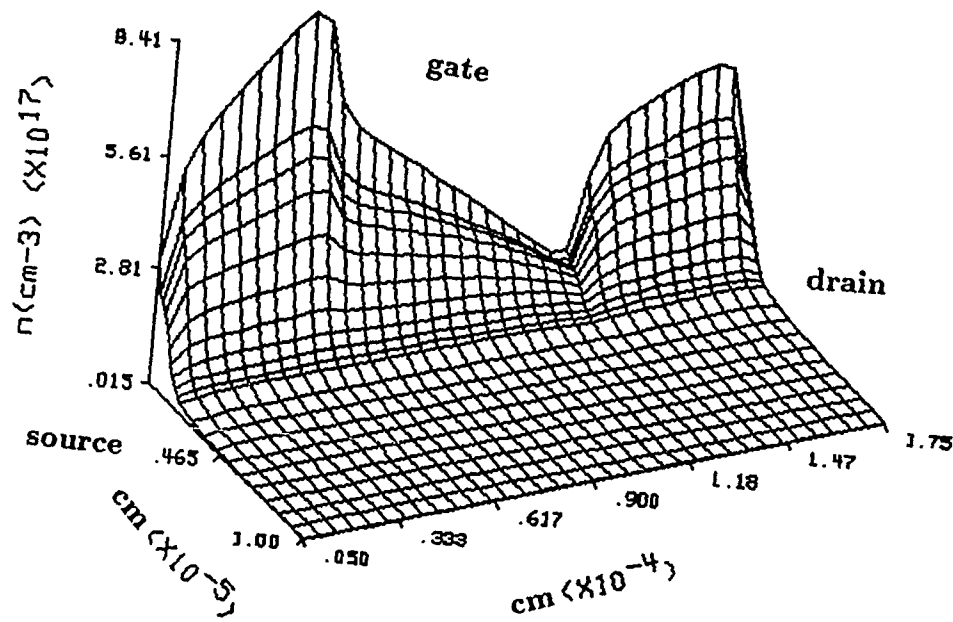


Figure 4.17: Total electron concentration in Device II with a gate voltage of 0.5V and a drain voltage of 0.9V

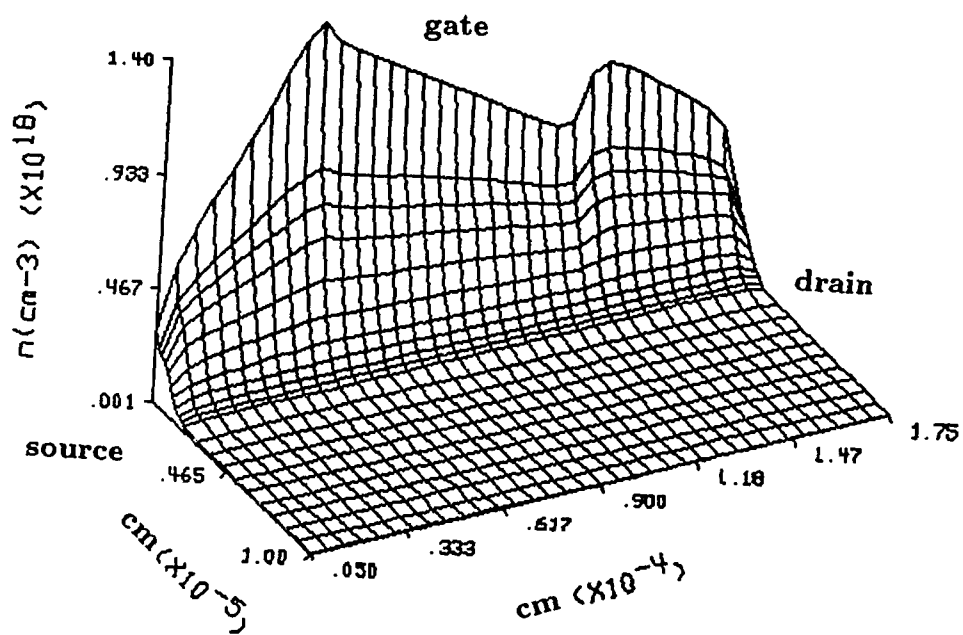


Figure 4.19: Total electron concentration in Device II with a gate voltage of 1.0V and a drain voltage of 0.9V

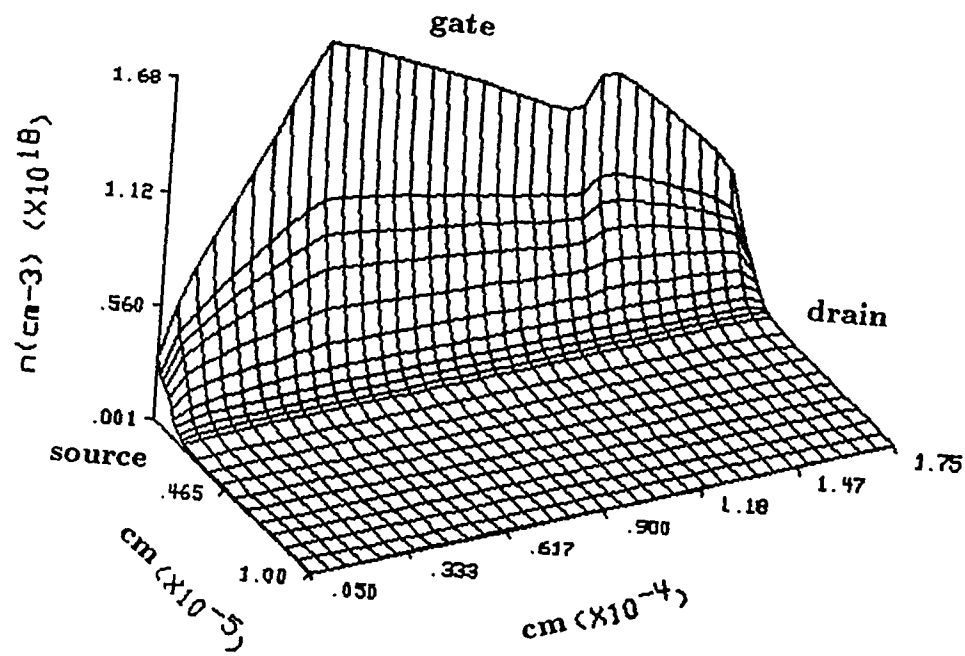


Figure 4.20: Total electron concentration in Device II with a gate voltage of 1.25V and a drain voltage of 0.9V

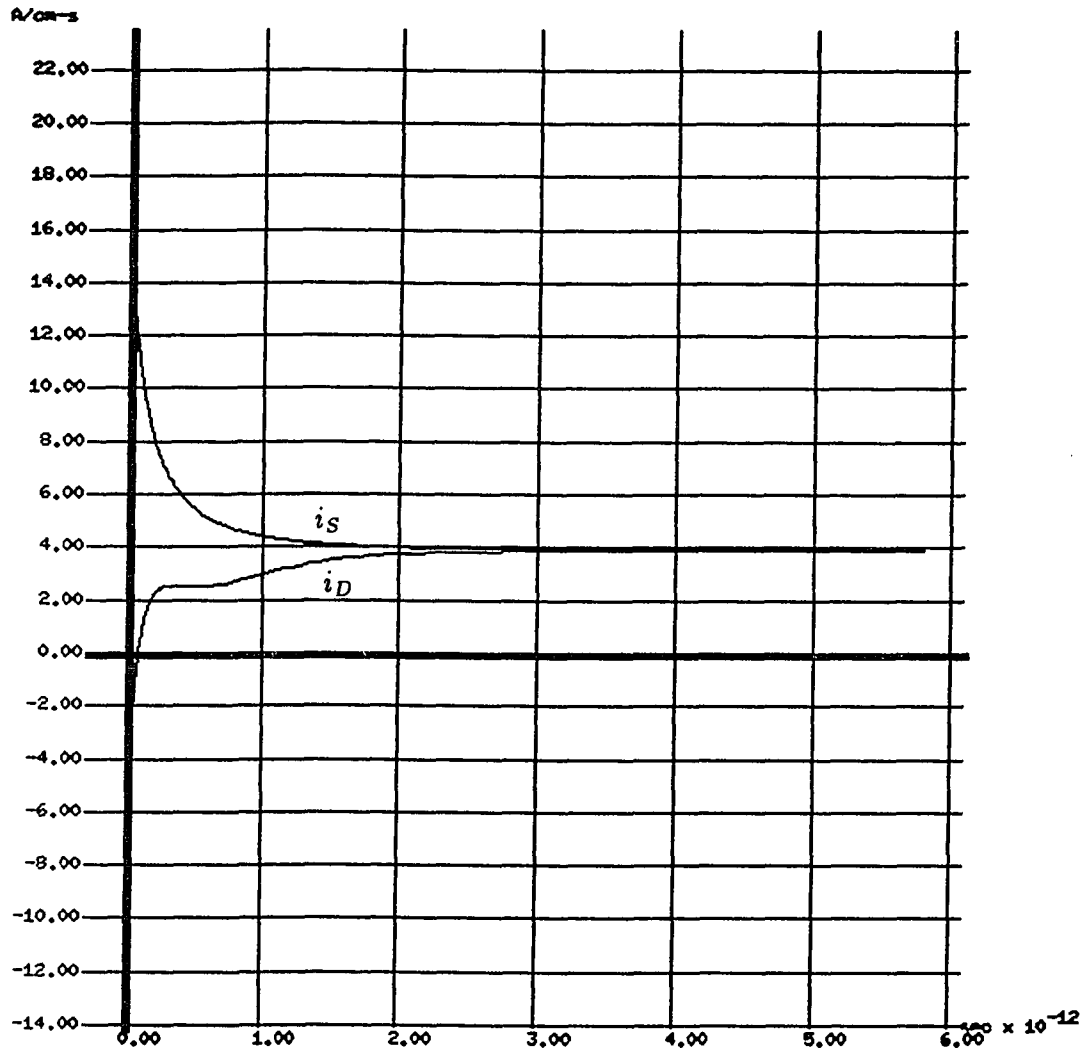


Figure 4.21: Transient currents for Device II with a gate voltage of 0.5V and a drain voltage of 0.9V

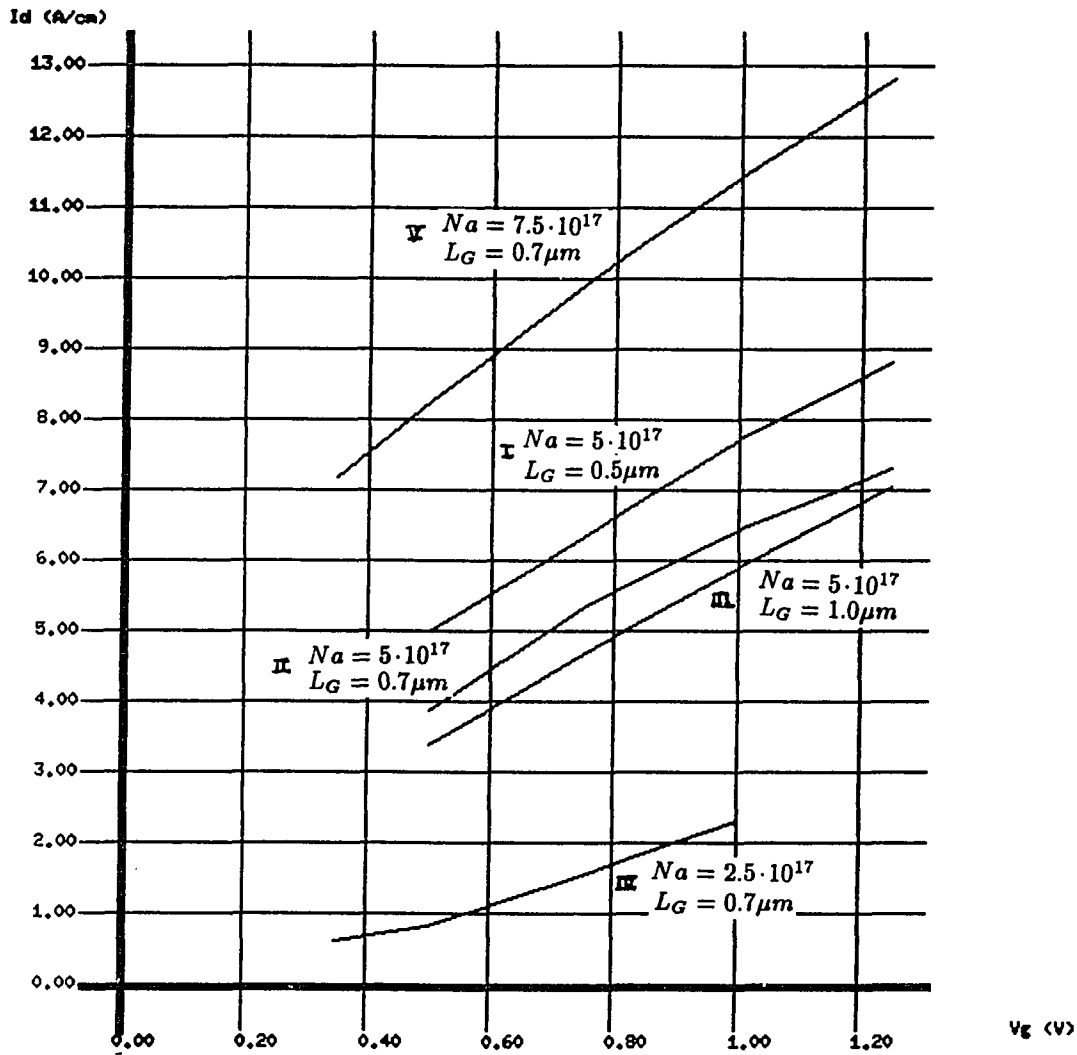


Figure 4.22: Drain current-gate voltage characteristic for Devices I-V under a drain voltage of 1.0V

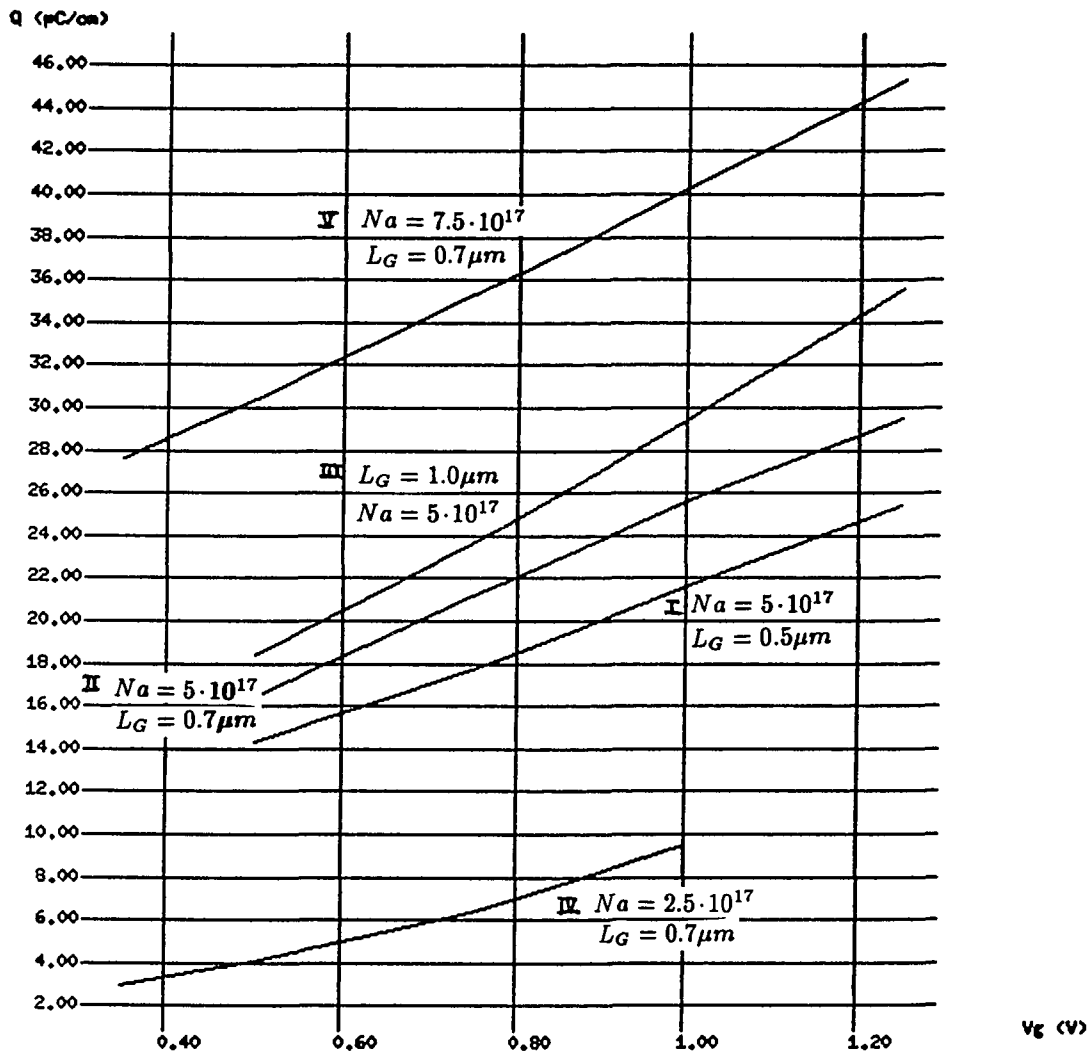


Figure 4.23: Charge-gate voltage characteristic for Devices I-V under a drain voltage of 1.0V

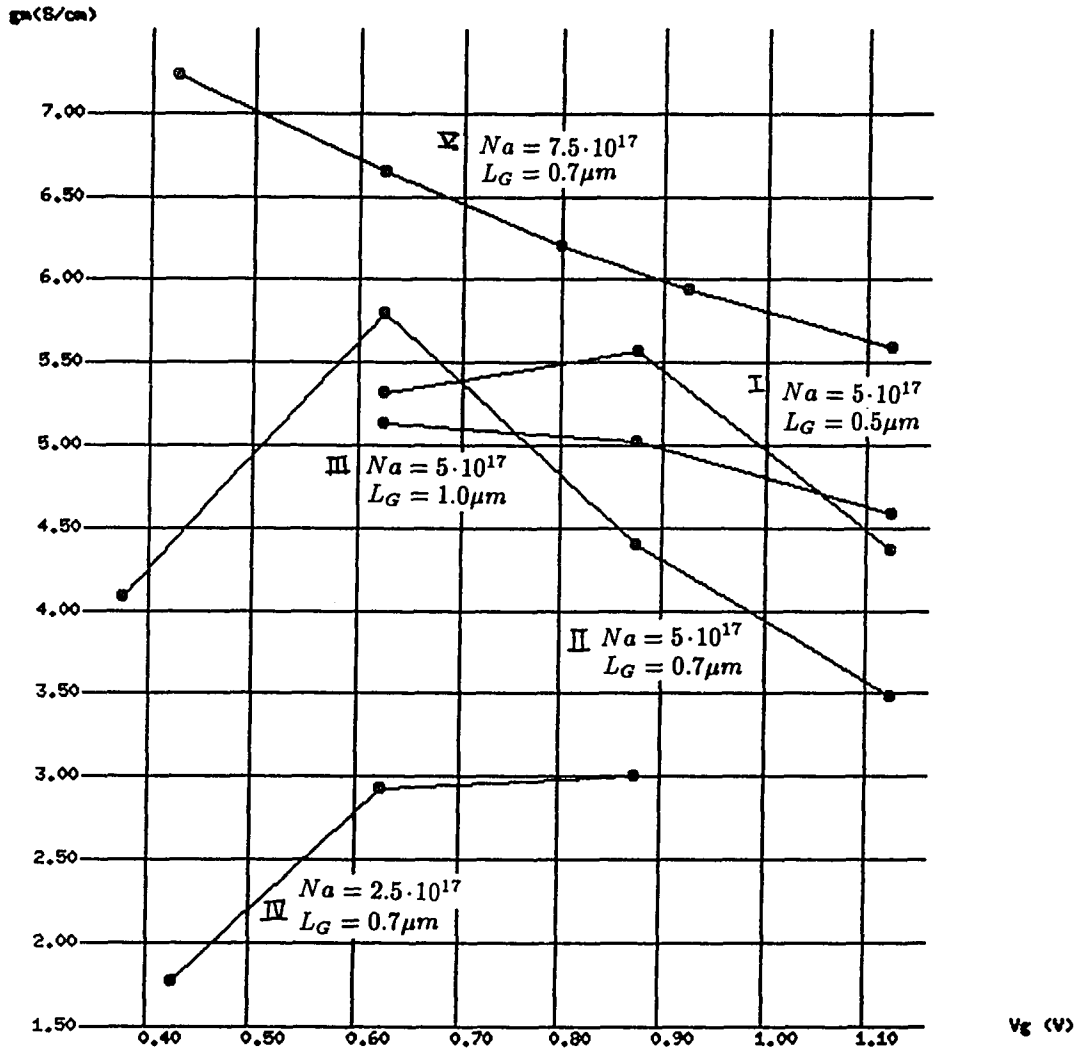


Figure 4.24: Transconductance for Devices I-V under a drain voltage of 1.0V

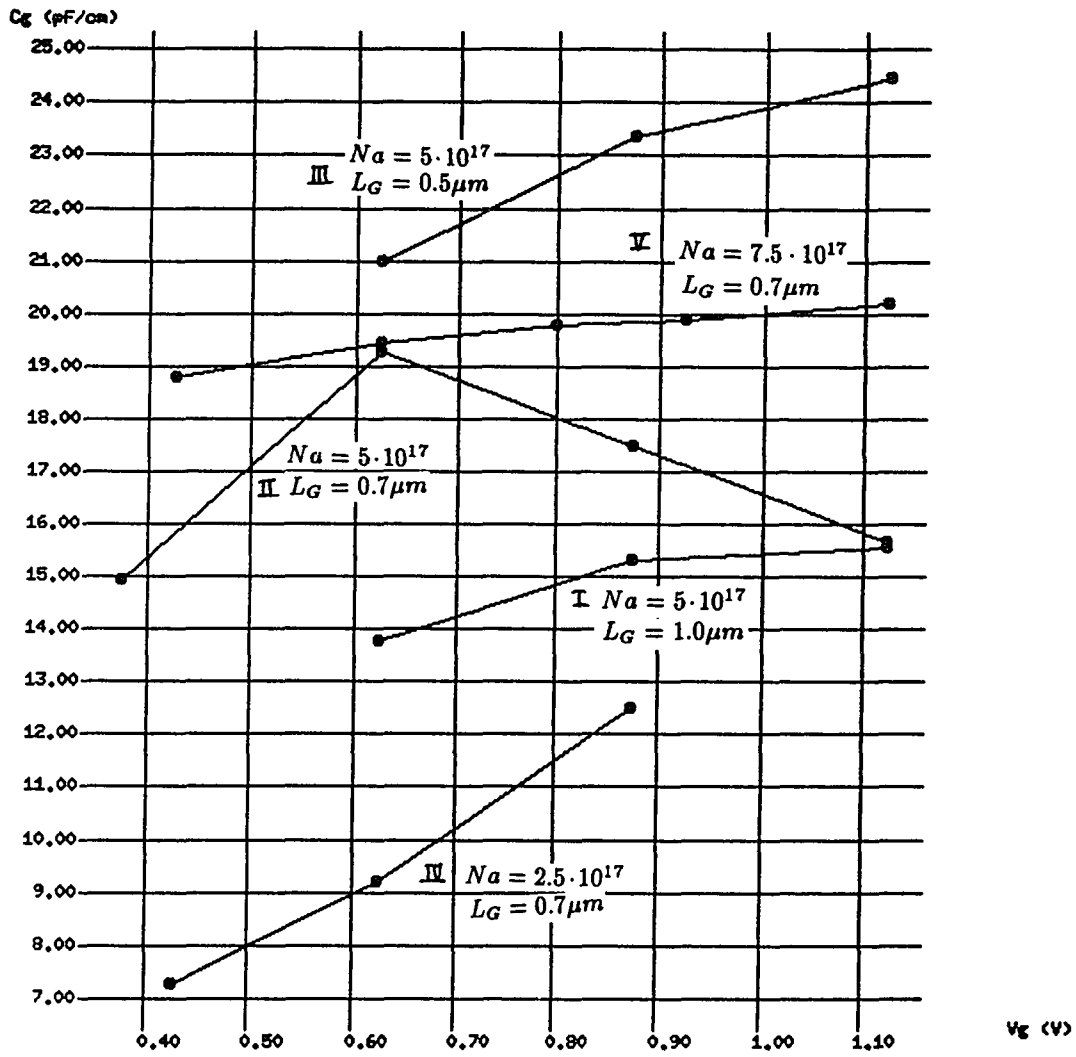


Figure 4.25: Gate capacitance for Devices I-V under a drain voltage of 1.0V

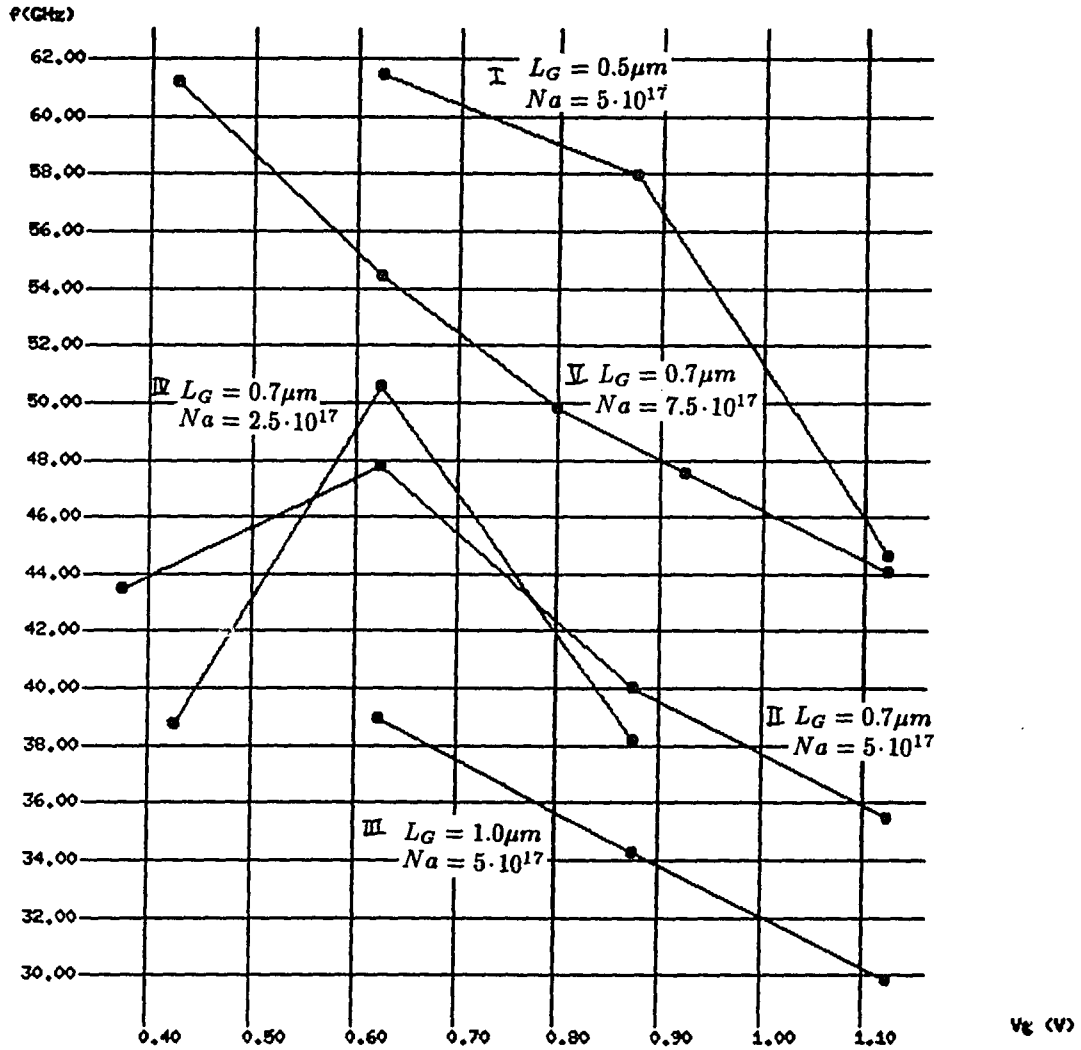


Figure 4.26: Unity-gain frequencies for Devices I-V under a drain voltage of 1.0V

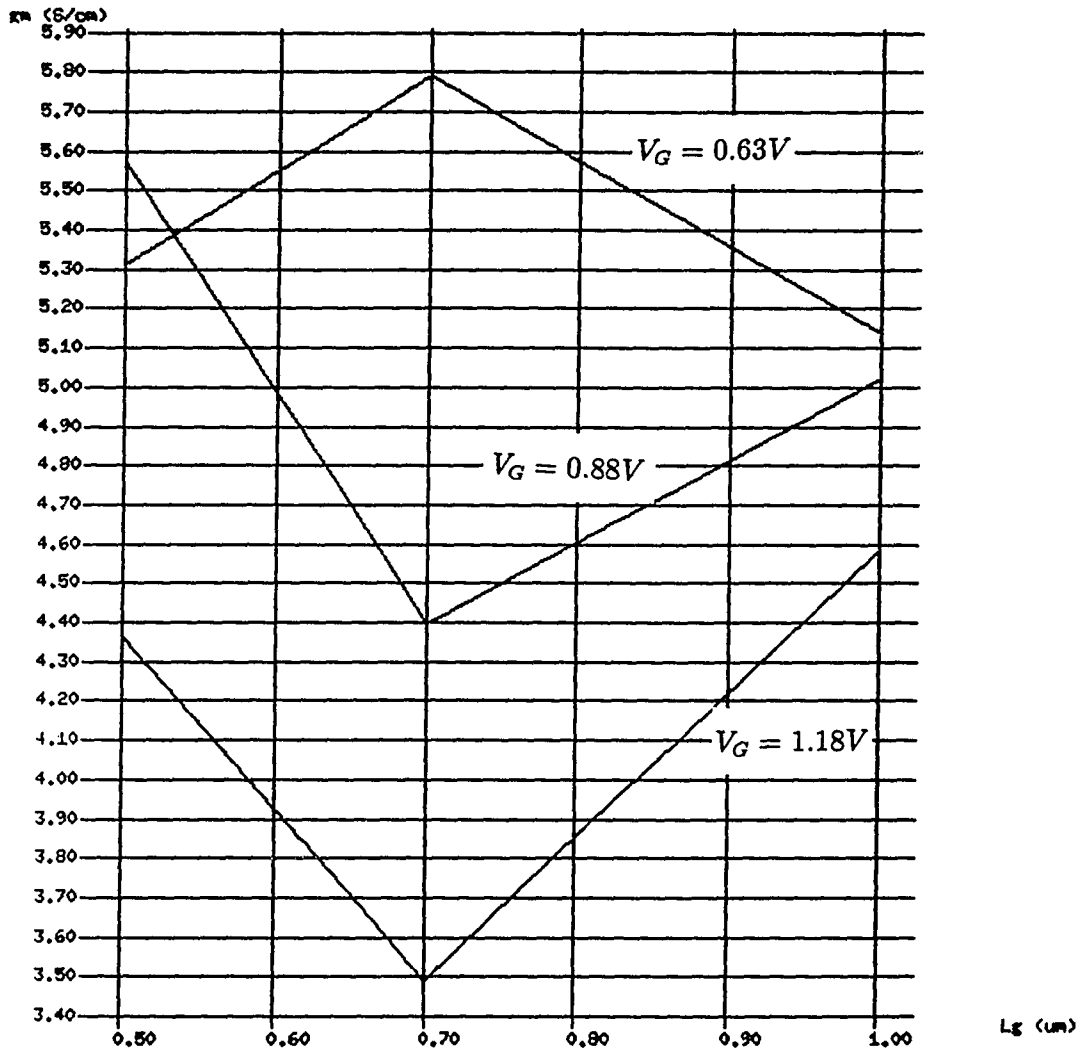


Figure 4.27: Variation of transconductance with the gate length

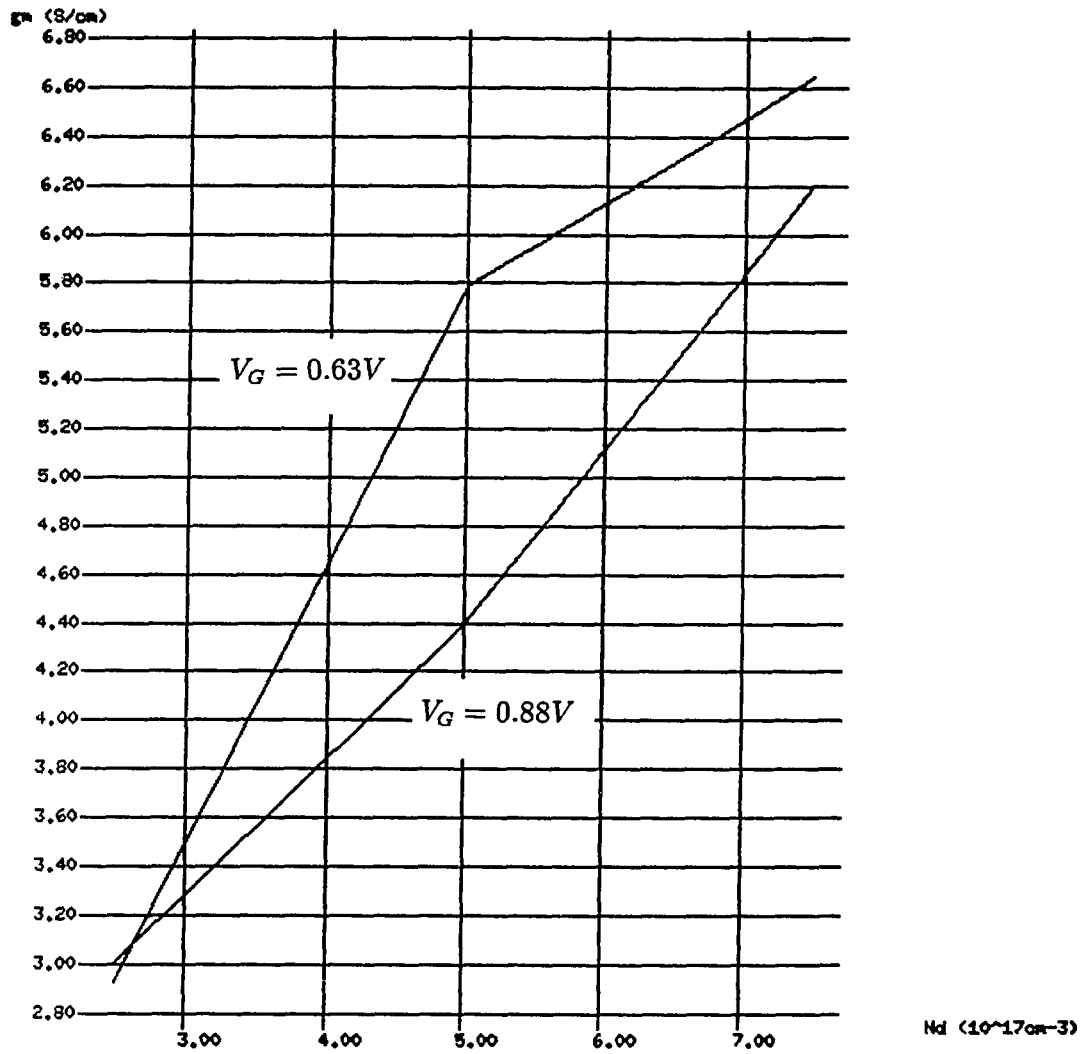


Figure 4.28: Variation of transconductance with the doping level

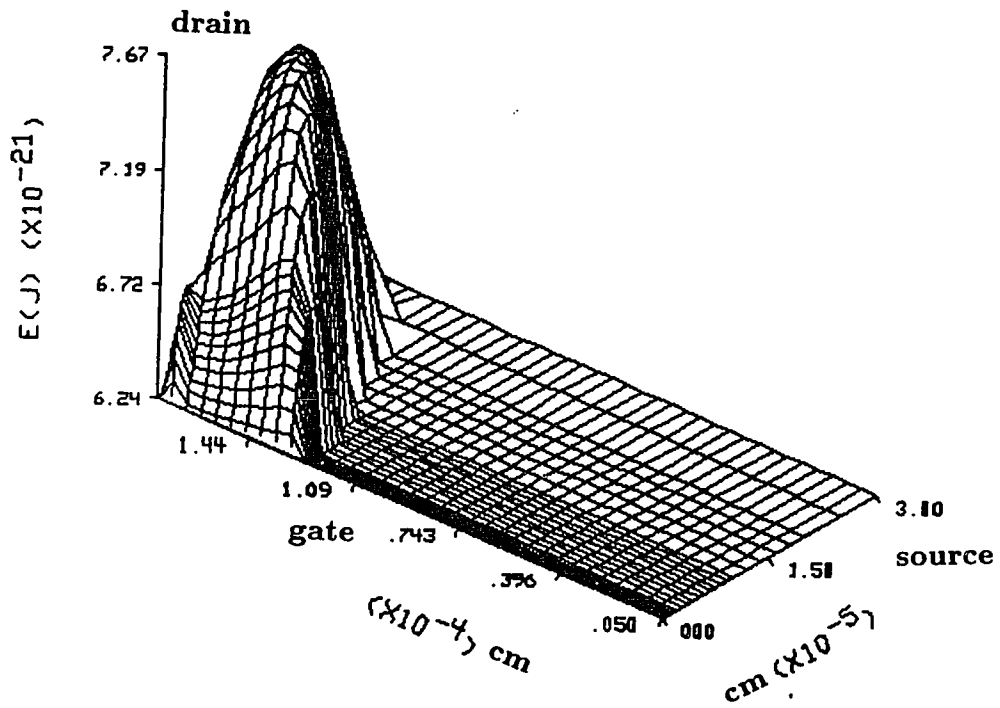


Figure 4.29: Average energy for Device VI with a gate voltage of 0.35V and a drain voltage of 1.0V

Reference

1. T. Mimura, K. Joshin, S. Hiyamizu, K. Hikosaka, and M. Abe, "High electron mobility transistor logic," **Japan J. Appl. Phys.**, vol. 20, pp. L598-600, 1981.
2. N. T. Linh, P. N. Tung, D. Delabeaudeuf, P. Delescluse, and M. Lavi-iron, "High speed-low power GaAs/AlGaAs TEGFET integrated circuit," **IEDM Tech. Dig.**, pp. 582-585, 1982.
3. J. V. DiLorenzo, R. Dingle, M. Feuer, A. C. Gossard, R. Hendel, J. C. M. Huaung, A. Kastalsky, V. G. Keramidas, R. A. Keihl, and P. O'Connor, "Material and device considerations for selectively doped heterojunction transistor," **IEDM Tech. Dig.**, pp. 578-581, 1982.
4. N. J. Shah, S. S. Pei, C. W. Tu, and R. C. Tiberio, "Gate-length dependence of the speed of SSI circuits using submicrometer selectively doped heterostructure transistor technology," **IEEE Trans. Electron Devices**, vol. ED-33, pp. 543-547, 1986.
5. J. Y.-F. Tang, "Two-dimensional simulation of MODFET and GaAs gate heterojunction FET's," **IEEE Trans. Electron Devices**, vol. ED-32, pp. 1817-1823, 1985.
6. D. J. Widiger, Ph.D. dissertation, University of Illinois, Urbana, Illinois, 1984.
7. D. Delagebeaudeuf and N. T. Linh, "Charge control of the heterojunction two-dimensional electron gas for MESFET application," **IEEE Trans. Electron Devices**, vol. ED-28, pp. 790-795, 1981.

8. D. Delagebeaudeuf and N. T. Linh, "Metal-(n) AlGaAs-GaAs two-dimensional electron gas FET," *IEEE Trans. Electron Devices*, vol. ED-29, pp. 955-960, 1982.
9. T. J. Drummond, H. Morkoc, K. Lee, and M. Shur, "Model for modulation doped field effect transistor," *IEEE Trans. Electron Device Lett.*, vol. EDL-3, pp. 338-341, 1982.
10. K. Lee, and M. Shur, T. J. Drummond, H. Morkoc, "Low-field mobility of 2-d electron gas in modulation-doped AlGaAs layers," *J. Appl. Phys.*, vol. 54, pp. 6432-6438, 1983.
11. D. J. Widiger, I. C. Kizilyalli, K. Hess, and J. J. Coleman, "Two-dimensional transient simulation of an idealized high electron mobility transistor," *IEEE Trans. Electron Devices*, vol. ED-32, 1092-1102, 1985.
12. D. Loret, "Two-dimensional numerical model for the high electron mobility transistor," *Solid-State Electronics*, vol. 30, pp. 1197-1203, 1987.
13. C. Jacoboni and L. Reggiani, "The Monte Carlo method for the solution of charge transport in semiconductors with applications to covalent materials," *Reviews of Modern Physics*, vol. 55, pp. 645-705, 1983.
14. P. Lugli, "The Monte Carlo method: application to semiconductor transport and process simulation," Tutorial given in SPIE conference on Advances in Semiconductors and Superconductors, Newport Beach, California, 14 March 1988.

15. T. Wang and K. Hess, "Calculation of the electron velocity distribution in high electron mobility transistor using an ensemble Monte Carlo method," *J. Appl. Phys.*, vol. 57, pp. 5336-5339, 1985.
16. M. Tomizawa, A. Yoshii, and K. Yokoyama, "Modeling for an Al-GaAs/GaAs heterostructure device using Monte Carlo simulation," *IEEE Electron Device Lett.*, vol EDL-6, pp. 332-334, 1985.
17. P. Price, "Low temperature two-dimensional mobility of a GaAs heterolayer," *Surface Sci.*, vol. 143, pp. 145-156, 1984.
18. P. Price, "Electron transport in polar heterolayers," *Surface Sci.*, vol. 113, pp. 199-210, 1982.
19. W. Walukiewicz, H. E. Ruda, J. Lagowski, and H. C. Gatos, "Electron mobility in modulation doped heterostructure," *Phys. Rev. B*, vol. 30, pp. 4571-4582, 1984.
20. K. Yokoyama and K. Hess, mentioned as private communication in the next reference.
21. U. Ravaioli and D. Ferry, "MODFET ensemble Monte Carlo model including the quasi-two-dimensional electron gas," *IEEE Trans. Electron Device*, vol. ED-33, pp. 677-680, 1986.
22. J. Yoshida, "Classical versus quantum mechanical calculation of the electron distribution at the n-AlGaAs/GaAs heterointerface," *IEEE Trans. Electron Device*, vol. ED-33, pp. 154-156, 1986.
23. R. Stratton, "Diffusion of hot and cold electrons in semiconductor barriers," *Phys. Rev.*, vol. 126, pp. 2002-2014, 1962.

24. C.-T. Hsing, Ph.D. dissertation, Univ. of Florida, Gainesville, Florida, 1977.
25. S. H. Gould, *Variational methods for eigenvalue problems*, second ed., Univ. of Toronto Press, 1957.
26. C. M. Snowden, *Introduction to semiconductor device modelling*, World Scientific, 1986.
27. M. Reiser, "A two-dimensional numerical FET model for dc-, ac- and large-signal analysis," *IBM Research J.*, RZ 499, April 1972.
28. K. Yokoyama and H. Sakaki, "Importance of low-field drift velocity characteristics for HEMT modeling," *IEEE Electron Device Lett.*, vol. EDL-8, pp.73-75, 1987.
29. K. L. Priddy, D. R. Kitchen, J. A. Grzyb, C. W. Litton, T. S. Henderson, C.-K. Peng, W. F. Kopp, and H. Morkoc, "Design of enhanced Schottky-barrier AlGaAs/GaAs MODFET's using highly doped p^+ surface layers," *IEEE Trans. Electron Devices*, vol. ED-34, pp. 175-179, 1987.
30. J. Waldrop, "Schottky-barrier height of ideal metal contacts to GaAs," *Appl. Phys. Lett.*, vol. 44, pp. 1002-1004, 1984.
31. G. D. Smith, *Numerical methods for partial differential equations: finite difference method*, Oxford, Clarendon Press, 1978.
32. V. I. Fistul, *Heavy Doped Semiconductors*, New York, N. Y., Plenum Press, 1969.

33. I. C. Kizilyalli, K. Hess, J. L. Larson, D. J. Widiger, "Scaling properties of high electron mobility transistor," **IEEE Trans. Electron Devices**, vol. ED-33, pp. 1427-1432. 1986.